SIMPLIFICATION OF MATHEMATICAL MODELS FOR MEDICAL ULTRASOUND POROELASTICITY IMAGING

A Dissertation

by

SANJAY PADMANABHAN NAIR

Submitted to the Office of Graduate and Professional Studies of
Texas A&M University
in partial fulfillment of the requirements for the degree of

DOCTOR OF PHILOSOPHY

Chair of Committee,	Raffaella Righetti
Committee Members,	Steven Wright
	Sebastian Hoyos
	Sevan Goenezen
Head of Department,	Miroslav Begovic

December 2016

Major Subject: Electrical Engineering

ABSTRACT

The use of an understanding of mechanical properties of tissues for the purposes of medical diagnosis has been going on since the foundation of the medical field as a science. In recent decades, medical ultrasound elastography techniques have been developed and improved and have helped the medical community improve the state of diagnosis and tracking of various diseases like cancer, and lymphedema. Poroelastography, refers to the extension of ultrasound elastography techniques towards imaging the mechanical properties of tissues that are modeled as poroelastic.

Currently, the field of poroelastography is stuck, largely due to the complication in the mathematical models surrounding poroelastic materials. This dissertation focuses on the investigation of the suitability of a simplified equation involving a single saturating exponential (i.e. time constant curve) to describe the local time-dependent strain response of non-homogeneous poroelastic materials placed under creep compression. A new algorithm of measuring how precisely a non-linear equation fits a set of data samples from an experiment, the Resimulation of Noise (RoN) algorithm, was developed and implemented for the time constant curve case. The RoN algorithm was shown to track the precision of the fit in a more intuitive and accurate manner than previously used quality of fit metrics.

The RoN algorithm coupled with an in-depth FEM simulation study was conducted to see how well the single exponential time-constant curve fit the localized strain samples of a simulated prismatic phantom with a cylindrical inclusion under different permeability and stiffness contrasts. The study showed that, on average, the single exponential time constant curve was suitable within 10% precision for 90% of the phantom's area so long as a mean-mask filter was applied the localized strain

images before attempting the curve-fit.

Future work in the field of poroelasticity imaging should center around the use of the single exponential time constant curve. This will require the development of a full understanding of how poroelastic material parameter contrast affects the contrast of the measured time constants. Procedures that will help this endeavor: such as the parallelization of the RoN algorithm as well as the development of novel non-homogeneous poroelastic phantoms with the aid of 3-d printers are also proposed.

DEDICATION

This work is the final expression of a very long campaign to improve the state of health and well-being of human life in this Earth. It is dedicated to everything that is good in the hearts of children, men, and women that makes us desire to keep their hearts beating and their faces smiling.

ACKNOWLEDGEMENTS

A comprehensive work like the one shown in this dissertation is never the product entirely of the author. What follows is my acknowledgment of who provided what to make this work a completed reality.

The scientific findings shown in this dissertation are the result of the guidance provided to me by Dr. Raffaella Righetti. She has mentored me with kindness, strength and keen scientific observation for almost a decade. I'm not entirely sure how it is that she managed to put up with me for that long, but she did and that is a good thing.

Anuj Chaudhry, Biren Parmar, Xu Yang, and yes, even Shafeeq Shajudeen, provided much of the laughter, camaraderie and alternative points of view that works like this always require. *Carlos Mejia, Tatiana Nuñez*, and Justin Parks provided much of the joy and emotional outlet required to properly function. The Everitt family provided countless pans of lasagna and well-wishes which were required during my final and stressful PhD years.

My amma, achan and Gautham provided me.

I want to close by expressing the joy I feel to say that I am a Texas Aggie through and through. I came in to this university a boy who just turned 18 and am leaving it a man at 31. I came in dubious, timid and weak and am feeling now reliable, confident, and strong and with my boots on. This place has been an alma mater in its latin sense and I am about to face the test of living an adult life. So as the song says, put a penny on ol' Sully and wish me some luck.

TABLE OF CONTENTS

LIST OF FIGURES

LIST OF TABLES

1. INTRODUCTION

1.1 Purpose

The purpose of this study is to investigate simplification of mathematical models of time dependent behaviors of strain for non-homogeneous poroelastic materials with the intent of using simplified mathematical models for medical ultrasound poroelasticiy imaging applications.

1.2 Mathematical modeling of tissue mechanics

Hidden in our understanding of mechanical properties is the fact that mechanical properties are merely parameters in the mathematical model which is chosen to model the physical behavior of tissues. Mathematical models are a tool by which we understand the relationships between observable physical phenomena. They are a balancing act between convenience and veracity. The more complex a model assumed, the higher its potential to unveil further information about the tissue. However, the complexity creates an added overhead in its difficulty of interpretation.

Currently, the most clinically imaged mechanical property of interest is the tissue's stiffness when the it is modeled as a linearly elastic (Hookean) solid [38]. In a hooken solid, the strain experience by the tissue is directly proportional to the stress following Hooke's Law (equation 1.1) [69]:

$$\sigma = -c\epsilon \tag{1.1}$$

In this equation σ is the stress tensor, ϵ is the strain tensor and c is a tensor containing the various coefficients of linear elasticity. What is commonly referred to as the "stiffness" of a tissue is an element of the tensor c known as the Young's

modulus and represents the linear coefficient of proportionality between the axial element of the strain tensor and the stress tensor.

While the model is simple, it has found itself to be very useful as Hookean elastography has a rich variety of clinical applications [20, 27, 77, 59]. However, it should be mentioned that few tissues, and in fact few materials truly behave as a linearly elastic solids under any circumstances. The assumption that a material behaves as a Hookean, homogeneous and isotropic material is generally acceptable so long as time dependencies are not considered and the stress and strain are both small [69]. In reality, all materials deviate from Hooke's Law [42]. While the model is extremely useful, the full potential of mechanically based diagnostic imaging can be untapped using more complex models. Merely considering non-linear elasticity has shown the potential of being a useful tool for the diagnosis of cancer [28]. The true potential of mechanical property based imaging lies in considering time-dependent behavior of tissues' response to mechanical excitation.

A viscoelastic material is one that is observed to exhibit both viscous and elastic characteristics. Viscous materials resist shear flow and strain linearly with time when a stress is applied. A viscous fluid under shear stress obeys the relationship $\sigma = \eta_v \frac{d\epsilon}{dt}$ with η_v being the viscosity of the fluid. In other words, a viscous materials resists the change of strain, while an elastic material resists strain.

To a certain extent, all materials, display viscoelastic tendencies [69]. Referring to ones own empirical observations is sufficient enough as proof to this as when a force is applied onto any material, the material does not instantly reach a final state of compression but reaches it over time. Tissues are no exception to this and the modeling of tissues as viscoelastic is currently revealing itself to be useful despite the fact that its methods are more complicated than those applicable to non time-dependent modeling [87, 57, 73, 68].

Perhaps the model with the highest potential to fully understand tissues is the poroelastic model [18]. Poroelastic materials are modeled as porous and elastic biphasic materials in which there is a solid linearly elastic matrix or skeleton that is coupled with a fluid phase (known as interstitial fluid). Frequently, sponges are referenced as a good example of poroelastic materials. Mechanically speaking, the defining characteristic of poroelastic materials is that the pore fluid pressure contributes to the total stress in the pores.

While the origins of the study of porous media are in the study of soil mechanics [79], its study is extremely relevant to tissue mechanics. In principle almost all tissues should technically be considered as poroelastic because all tissues in multicellular animals are bathed in interstitial fluid which transports nutrients or waste products. The flow of this fluid through tissue is a requirement for it to remain healthy. Because of this the imaging of poroelastic parameters holds a key to powerful diagnostic imaging because poroelastic materials closely describe tissues.

However, as mentioned earlier, for a mathematical model to more closely describe observed behavior, it almost always comes at the cost of increased mathematical complexity. While, indeed, current research has shown that there is tremendous potential in diagnosis by observing the poroelastic properties of tissue [38, 47, 14, 6, 4, 5, 1, 40, 61, 62, 63, 64, 65], the mathematics involved in poroelasticity imaging are considerably complex. Indeed, the field of poroelasticity imaging has considerably stagnated. *The work compiled in this dissertation is a concentrated effort towards simplifying the mathematics for the purposes of accelerating the development of clinical ultrasound poroelasticity imaging.*

1.3 Background on ultrasound elastography

As of this writing, Ultrasound elastography comprises a family of well-established imaging modalities used to, in some way or the other gain an understanding of the mechanical properties of tissues [72, 84]. Gaining an understanding of underlying mechanical properties of tissues has been known to be diagnostically relevant for centuries [84]. All ultrasound elastographic modalities involve the application of a mechanical stimulus or stress followed by a the measurement of the tissue's response to that stimulus. Perhaps the most clinically used ultrasound elastography modalities used to date are quasistatic strain imaging and shear wave elasticity imaging (SWEI) [84, 72].

In SWEI the mechanical stimulus is provided by an acoustic radiation force that creates shear waves that can be detected by acoustic ultrasound [72, 52]. The deformations to this tissue are then measured and are used for mechanical characterization [52]. A special type of SWEI, supersonic shear imaging (SSI) which is currently available in the Texas A&M Ultrasound group, directly measures the speed of shear waves in the mechanical tissues and uses this to directly image mechanical properties of tissues [78, 19].

Quasistatic strain imaging is perhaps the first of the clinically available forms of Ultrasound Elastography. Indeed, the term elastography, was first coined for this imaging modality [54, 53, 80, 81]. Quasistatic strain imaging involves collecting an ultrasound RF-frame of the tissue to be imaged before compression and then another one after compression has been completed. Using cross-correlation techniques, the RF-frames are then compared in order to calculate localized displacements. The localized strains experienced by the tissue are then calculated by taking the gradient of the displacement image.

4

The work compiled in this dissertation regards the extension of quasistatic ultrasound elastography for the purposes of imaging the poroelastic mechanical properties. While it is true that SWEI imaging modalities are arguably easier to use than quasistatic ultrasound elastography, the interpretation of the images produced requires a presupposition of the mathematical model the tissue is assumed to follow. Strain measurements, on the other hand, are not tainted by any prior assumptions on mathematical models.

1.4 Mathematical complications of ultrasound poroelasticity imaging

With quasistatic ultrasound elastography, one has access to only a few measurements: axial strain, lateral strain, effective Poisson's ratio (EPR) and shear-strain [54, 39, 37]. This means that the poroelastic parameters of tissues need to be analyzed with only these four measurements and preferably with only one: axial strain as its higher resolution provides for better image quality [66]. However, understanding the poroelastic properties of tissues through observing axial strain is complicated.

Consider the findings in Armstrong et. al [2]. Armstrong showed a theoretical derivation of the strain vs time behavior of a homogeneous isotropic cylindrical poroelastic material under creep compression. Under creep compression the strain vs time behavior is shown in 1.2.

$$\epsilon_{zz}(t) = -\frac{F_0}{E_s \pi a^2}[1 - (1 - \nu_s^2)(1 - 2\nu_s)\sum_{n=1}^{\infty}\frac{4}{9(1 - \nu_s)^2\beta_n^2 - 8(1 + \nu_s)(1 - 2\nu_s)}e^{-\beta_n^2 \frac{H_A kt}{a^2}}$$

(1.2)

As can be observed equation 1.2 involves an infinite number of parameters, however of special note are the Young's Modulus of the solid matrix (E_s), the Poisson's Ratio of the solid matrix (ν_s) and the permeability of the material (k). It is interest-

ing to note that equation 1.2 shows that the time dependent strain response of this material under creep compression is characterized by an infinite sum of saturating exponentials. Berry et al [4] extended this derivation and found that the localized strain vs time behavior of a cylindrical tissue follows a similar pattern.

As complicated as equation 1.2 might appear to be, there were assumptions that were made to symplify its derivation. The derivation was made for a cylindrical and homogeneous poroelastic material. While the assumption is convenient and useful, it is worth noting that it voids the necessity for imaging. Medical imaging is presupposed on the belief that the area being imaged is non-homogeneous. Despite this, perhaps the biggest problem with the expression for $\epsilon_{zz}(t)$ is that it is too complicated. Attempting to characterize a poroelastic material from its strain response would require the estimation of an infinite number of parameters. It is clear that, in order to gain insight on the poroelastic parameters of non-homogeneous tissues, a simpler strain vs time relationship than shown in equation 1.2 needs to be studied.

1.5 Hypothesized solution and aims

The work compiled in this dissertation aims to see if it is possible to reduce equation 1.2 to a single saturating exponential as shown in equation 1.3:

$$\epsilon_{zz}(t) = \eta + (\alpha - \eta)e^{-\frac{t}{\tau}} \tag{1.3}$$

where η is known as the equilibrium point (EP) τ is known as the time constant (TC) and α is the value of $\epsilon_{zz}(t)$ when $t = 0^+$. Equation 1.3 is often referred to as a time constant curve.

To test the proposed hypothesis, the following aims needed to be executed:

1. Examine the fit of single exponential time constant curves to local temporal elastographic data for non-homogeneous poroelastic media.

6

(a) Develop a goodness-of-fit measure specialized for non-linear curve-fitting.

(b) Examine the goodness-of-fit of TC curves to local temporal elastographic data for non-homogeneous media.

2. Investigate the possibility of using single exponential time constant curves to determine permeability and Young's Modulus contrasts for non-homogeneous poroelastic media.

Hidden in this aims is the fact that this work has to tackle a lot of complexities with regards to Least Square Error estimation non-linear equations which are often taken for granted [29]. Indeed, the first few chapters of this dissertation deal entirely on this subject and should have applications well beyond poroelasticity imaging as the use of non-linear least square error parameter estimation is ubiquitous [86, 44]. As Least Square Error estimation is central to this dissertation, the next chapper reviews some of the more notable results from my MS work that are necessary for understanding this work.

2. REVIEW OF LEAST SQUARE ERROR ESTIMATION[*]

The work shown in this chapter was developed into my M.S. thesis and was then published in [51]. Since an understanding of non-linear least square error estimation is a requirement for the understanding of this dissertation, this chapter is included as a review of some of the important findings found earlier.

2.1   Introduction

Elastographic imaging of poroelastic and viscoelastic materials has been accomplished by generating time-sequenced axial strain elastograms or EPR elastograms while subjecting the material to a constant axial strain (stress relaxation) or a constant axial stress (creep). Given a set of temporal elastograms obtained from a poroelastic or viscoelastic material, it is possible to generate time constant elastograms, which provide information about the temporal behavior of the elastographic parameter of interest. Time constant elastograms are generated by applying mechanical models to the experimental elastographic data to estimate the TC of the elastographic parameter of interest on a pixel-by-pixel basis using curve-fitting techniques [63, 65, 57].

In general, a large number of theoretical models can be applied to creep or stress relaxation data to extract tissue poroelastic parameters and related time constants [70, 24]. However, not all of them may be of practical use in clinical situations. In the past, poroelastographic data have been interpreted using the model that employs the Kuei, Lai, and Mow biphasic theory [2] to predict the time-dependent radial or axial strain in poroelastic materials in unconfined compression [63, 4, 5].

---

[*] ©2011 IEEE. Reprinted, with permission, from Nair SP, Yang X, Krouskop TA, Righetti R, Performance analysis of a new real-time elastographic time constant estimator, IEEE:Transactions in Medical Imaging, Feb 2011

The application of this model was found to be useful. The application of this model was found to be useful to develop poroelastographic simulation methods [64, 4] and also to approximate selected experimental data in vitro [63, 4]. Currently, however, this model has not been applied directly to elastographic data in vivo, presumably due to its complexity, the difficulty in reproducing experimental conditions that are consistent with the assumptions of the model and the inevitable challenges encountered in describing complex and heterogeneous poroelastic tissues.

Simplicity and efficiency in the calculations, accuracy of approximation and applicability to a broad field of materials are key parameters that need to be considered when developing an estimator that may be of use in clinical applications [70]. It is in this context that the idea to approximate creep or stress relaxation data using simple exponential polynomials has been evaluated as an attractive alternative [4, 70, 62, 48]. Within the class of exponential functions, models featuring only a single exponential have been employed to estimate the temporal behavior of both tissues in vitro and in vivo with some success but not without compromises [63, 57, 61, 73] . Although these models may not be as fully descriptive as models that employ an infinite sum of exponentials, their analysis may serve as a foundation for the study of more complex models [70].

Regardless of the model that is used, elastographic TC imaging usually involves applying curve fitting methods to noisy elastographic data. The accuracy of the resulting TC estimates is expected to depend on the curve fitting method employed, the length of the window of observation, the sampling period used to acquire the elastographic data and the noise level in the elastographic data [3]. A complication that arises in the application of curve-fitting methods to poroelastography data is that, in practical cases, the models usually contain multiple parameters that need to be estimated due to the biphasic nature of the poroelastic tissues [67]. This observation

9

poses the problem of having to estimate multiple tissue parameters simultaneously from a set of noisy data acquired for a limited time interval.

The current literature on poroelastographic techniques is limited to a relatively small number of publications, which suggest their technical feasibility but do not comprehensively tackle difficult yet fundamental issues of clinical importance. While these studies [38, 64, 4] have certainly provided motivation to continue the development of poroelastographic methods, they have only started addressing the important issues of noise limitations inherent to temporal strain estimations (i.e., due to both temporal tracking and quality of strain estimates), poroelastographic image quality performance and the role of various practical temporal parameters in the resulting poroelastographic images. These important issues need to be investigated in a systematic manner if poroelastography is to become an established clinical imaging modality.

Furthermore, current implementations of poroelastography imaging methods are too slow and not optimized for clinical applications. Current poroelastography methods in vivo are based on the application of a constant strain compression and consequent generation of EPR elastograms [61] or, alternatively, of axial strain elastograms [6]. Methods that employ EPR elastograms only, are inherently noisy due to image quality limitations typical of lateral strain elastography [67]. While it is possible to use axial strain elastography to estimate the poroelastic behavior of tissues [4, 61], methods that employ only axial strain elastograms may not be able to determine if the observed temporal tissue behavior is due to viscoelastic or poroelastic effects [4, 71, 5]. Thus, EPR elastography should be used in combination with axial strain elastography to confirm the existence of any changes in tissue compressibility, which is characteristic of underlying fluid movements.

This chapter presents the results of a performance study of a time constant es-

timator for clinical elastography applications. The estimator uses the least square error (LSE) curve-fitting method and the Levenberg-Marquardt (LM) optimization rule as applied to noisy elastographic data obtained in creep experiments. The image quality performance of the estimator is analyzed in terms of accuracy, precision, sensitivity, signal to noise ratio (SNR), and speed. The use of this estimator provides a means to better understand and image the overall temporal behavior of complex tissue systems, for tissues that are assumed to be either poroelastic or viscoelastic.

2.2   Theoretical background

2.2.1   The least square error problem for single exponential time constant estimation

Let s be the elastographic parameter of interest. As a first order approximation, a simple and practical empirical model to describe the temporal mechanical behavior of s from a set of experimental temporal elastograms is given by [63, 61, 57]:

$$s(t) = \eta + (\alpha - \eta)e^{-\frac{t}{\tau}} \qquad (2.1)$$

where $s(t)$ is the value of the elastographic parameter of interest at time t, α is the value of s at time $t = 0^+$, η is the equilibrium point (EP) (i.e. $s(t \to \infty)$) and τ is the time constant (TC) of the elastographic parameter of interest. It should be reinforced that this model is much simpler than some of the models previously encountered in the literature that present the transient strain response under creep compression as an infinite sum of exponentials [2, 4]. Under certain assumptions imposed by the boundary conditions, the model in equation 2.1 may be used to approximate both the axial strain and the EPR temporal behavior [61]. In the axial strain case, as is studied in this dissertation, α is expected to be a value close to the applied axial strain.

While in a strict sense, α is a term that should also be estimated for proper LSE estimation, it can be treated as an a priori measurement because the level of noise affecting the strain estimate at $t = 0^+$ is always significantly smaller than the level of noise affecting all subsequent points [6, 62]. Historically, elastographic models have assumed that η could be estimated from the elastogram corresponding to the last acquired RF frame of the set [70]. This, however, would require acquisition of data for an infinite time. In addition, both τ and η are material-dependant and thus both of them should have important diagnostic value [63, 4, 57, 62]. This it is important to investigate if both τ and η can be estimated with accuracy, sensitivity and SNR that are acceptable for elastography applications [30, 83].

In practice, it is impossible to acquire $s(t)$ as described in 2.1. It is only possible to acquiare a series of m noisy samples of $s(t)$ due to the discrete nature of the ultrasonic acquisition and inevitable noise sources. Thus, a more useful representation of the model that can be used in the curve fitting expressions that represent the estimated temporal strain data may be given by:

$$s(t_i) = \eta + (\alpha - \eta)e^{-\frac{t_i}{\tau}} + N_i(t_i) \tag{2.2}$$

where $s(t_i)$ is the strain sample at time t_i and $N_i(t_i)$ is the noise level at time t_i. $N_i(t_i)$ is assumed to come from a zero-mean Gaussian noise distribution (i.e $N_i(t_i) \sim N(0, \sigma)$). Additive white Gaussian noise is a simple and commonly used noise model [76, 30]. The presence of this noise, however, poses the biggest challenge for the extraction of τ and η from the samples $s(t_i)$. For most of the cases studied, the noise model is assumed to have a constant SNR equal to $20\, dB$ for all strain samples. This value is in the range of expected SNR values for elastography applications [76]. Following the convention usually employed in signal and image processing

12

applications and in elastography, the SNR is measured as:

$$SNR(dB) = 20log(\frac{mean(s(t_i))}{std(s(t_i))}) \tag{2.3}$$

LSE curve-fitting is a well-known and largely applied method to extract parameters of a mathematical model from a given set of experimental data. In reference to equation 2.2, the application of LSE curve-fitting techniques aims at at finding the parameters $\hat{\tau}$ and $\hat{\eta}$ that minimize the LSE as shown in equation 2.4:

$$LSE(\hat{\tau}, \hat{\eta}) = \sum_{i=1}^{m}(s(t_i) - (\hat{\eta} + (\alpha - \hat{\eta})e^{-\frac{t_i}{\tau}}))^2 \tag{2.4}$$

It is worth noting that parameter extraction by means of LSE minimization is most valid under the condition that the samples' noise distributions follow independent and identical (iid) Gaussian distributions [12]. With respect to our model, a perhaps more accurate estimate would be obtained by minimization with respect to a weighted LSE (WLSE) function [43]:

$$WLSE(\hat{\tau}, \hat{\eta}) = \sum_{i=1}^{m}w_i(s(t_i) - (\hat{\eta} + (\alpha - \hat{\eta})e^{-\frac{t_i}{\tau}}))^2 \tag{2.5}$$

where w_i represents represent a measure of the weight given to the error at point i. However, minimization with respect to WLSE requires knowledge of all σ_i in order to assign values to w_i. Since, in the case of ultrasound elastography, σ_i is usually unknown a priori, the entire dissertation makes use only of standard LSE estimation.

Once the LSE problem is formulated, the challenge then becomes implementing an optimization rule to estimate τ and η. This optimization was implemented using the Levenberg-Marquardt optimization rule.

2.2.2 Levenberg-Marquardt optimization for single exponential time constant LSE estimation

The Levenberg-Marquardt (LM) optimization algorithm is an iterative algorithm based on gradient descent and the Newton method for finding equation roots, which is especially suited for LSE estimation [58]. Minimization with respect to equation the LSE as in equation 2.4 is equivalent to minimization with respect to:

$$E(\hat{\tau}, \hat{\eta}) = \frac{1}{2} \sum_{i=1}^{m} r_i^2(\hat{\tau}, \hat{\eta})) \qquad (2.6)$$

where $r_i(\hat{\tau}, \hat{\eta})$ is itself defined by equation 2.7.

$$r_i(\hat{\tau}, \hat{\eta}) = s(t_i) - (\hat{\eta} + (\alpha - \hat{\eta})e^{-\frac{t_i}{\tau}} \qquad (2.7)$$

The parameters $\hat{\tau}$ and $\hat{\eta}$ can be be vectorized as $x = [\hat{\tau}, \hat{\eta}]^T$. The LM optimization follows an update rule of the form [58]:

$$x_{k+1} = x_k - (H + \lambda \dot{diag}(diag(H)))^{-1} \nabla E(x_k) \qquad (2.8)$$

where $x_k = [\hat{\tau}_k, \hat{\eta}_k]^T$ is the current guess, H is the Hessian of $E(x_k)$, $diag(diag(H))$ denotes a diagonal matrix whose nonzero elements are the diagonal elements of matrix H, $\nabla E(x_k)$ is the gradient of $E(x_k)$, and λ is a constantly changing step size. In practice, λ is picked at each step using the following algorithm:

1. update x_k as indicated in equation 2.8

2. if $E(x_{k+1}) > E(x_k)$ then reject x_{k+1}, retract to x_k and increase λ by a factor of 10. Otherwise, accept x_{k+1} and decrease λ by a factor of 10.

14

2.3 Simulation procedure

A simulation study was performed to assess accuracy, precision, sensitivity, speed and SNR of the proposed LM algorithm as a function of the true strain TC and equilibrium points. due to the importance of the noise model on the estimation process, selected simulations were repeated for different values of the noise SNR. All simulations were performed in MATLAB. The simulations were performed by creating a series of temporal strain curves following 2.1 with known theoretical τ and η parameters. The maximum sampling rate was fixed at 2 samples per second. Such sampling rates are usually possible in practical elastography systems, which achieve typical frame rates of several frames per second [88]. It should be noted that low sampling rates adversely affect the estimator's performance, especially in the case of lower τ values. This implies that the sampling rate needs to be adjusted according to the true τ values as expected from the Shannon-Nyquist sampling theorem. Figure 2.1 shows an example simulation. In this figure, the dashed line represents the actual time constant curve as in equation 2.1 when $\tau = 150s$ and $\eta = 0.1$, the dots show the noisy samples $s(t_i)$ as in equation 2.2 and the solid line shows the estimated time constant curve when the noisy samples are input into the LSE LM estimator.

2.3.1 Evaluation of accuracy and precision

Accuracy and precision were measured in terms of percent deviation (i.e. percent bias) and percent spread, respectively [3, 35]. For a given set of n trial estimates $\hat{\tau}_i$, $1 \leq i \leq n$ performed on a set of noisy samples from a TC curve of known τ, the accuracy is quantified as a function of the percent bias as in equation 2.9. The precision is quantified in terms of the percent spread as in equation 2.10.

$$percent\,bias(\%) = \frac{|mean(\hat{\tau}_i) - \tau|}{\tau} \times 100 \qquad (2.9)$$
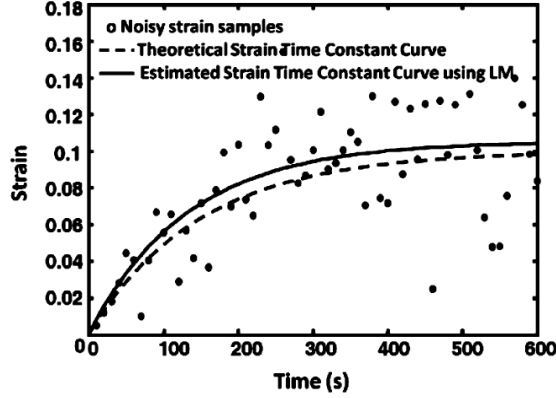
Figure 2.1: Example of a simulation trial using noisy samples and a corresponding estimated curve obtained using the LM LSE estimator when the actual $\tau = 150s$ and $\eta = 0.1$.

$$percent\ spread(\%) = \frac{std(\hat{\tau}_i)}{\tau} \times 100 \qquad (2.10)$$

In equation 2.9 std refers to the standard deviation.

Accuracy and precision were tested for true τ values in the range of $1 - 800s$ and for true η values in the range of $0.01 - 0.05$. While in the actual study two windows of observation were considered [51], for the purposes of summary, only the results of when the window of observation was $600s$ are shown. For the statistical analysis, 50 trials were run for each pair of true TC and equilibrium point values.

2.4   Results

2.4.1   Accuracy and precision

Figures 2.2 and 2.3 show the percent bias and percent spread, respectively, of the LM optimized LSE estimator for the simulation study described. These figures show that percent bias for a given window of observation is dependent on the underlying τ and in many cases is below 1%. A similar dependency to τ is observed for the percent spread but in most cases shows a percent spread of less than 5%.

16
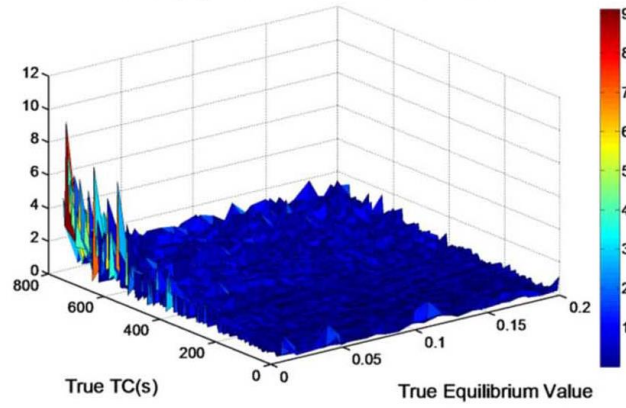
Figure 2.2: LM LSE estimator percent bias as a function of the true time constant and equilibrium point when the window of observation is $600s$
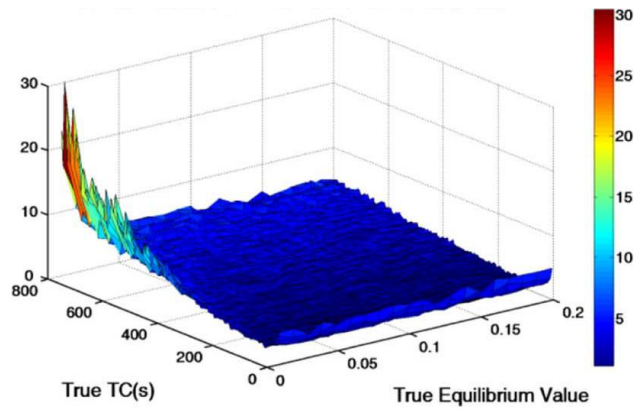
Figure 2.3: LM LSE estimator percent spread as a function of the true time constant and equilibrium point when the window of observation is $600s$

The figures show an observed deterioration in the precision and accuracy of the estimator for very low values of τ. This can be explained by observing the fact that as τ decreases the bandwidth of the time constant signal shown in equation 2.1 increases. As predicted by the Shannon-Nyquist theorem, this would require a higher sampling frequency for $s(t_i)$.

2.5 Discussion and conclusion

This chapter showed a thorough review and description of LSE estimation as applied to single exponential time constant curve fitting. Throughout the rest of this dissertation this LM optimized LSE estimator is analyzed thoroughly and used. While indeed other optimization schemes are readily available in the literature [9], the LM optimization was chosen because it is well suited for the LSE optimization problem [58]. Because they are so important throughout the rest of the work, many of the equations and findings shown in this chapter will be restated in subsequent chapters.

As mentioned earlier, the majority of this work was actually done during my M.S. and further details can be found in my M.S. thesis [48]. These findings were then formalized into a peer-reviewed journal publication [51]. These findings showed that the LM LSE estimator is substantially accurate and precise. Admittedly, that last statement is a blanketed one as the findings also showed that the performance of the LSE estimator is dependent on the underlying time constant, τ as well as the window of observation and the sampling frequency of the strain samples.

This dissertation is about addressing the suitability of describing the localized axial strain response of poroelastic media under creep compression as a single exponential time constant equation as shown in equation 2.1. This cannot be done without fully understanding the LM LSE performance dependencies mentioned earlier. These

dependencies needed to be studied and the next chapter of this dissertation deals with exactly that.

3. EFFECT OF TEMPORAL ACQUISITION PARAMETERS ON IMAGE QUALITY OF STRAIN TIME CONSTANT ELASTOGRAPHY

The work shown in this chapter was developed in conjunction with Joshua Varghese and Anuj Chaudhry. Indeed, a sizable portion of this work was developed into Joshua Varghese's M.S. thesis [82]. The early years of my PhD work were dedicated towards extending and formalizing the results shown in his thesis and were then published into a peer-reviewed journal publication [50].

3.1   Introduction

Ultrasound elastography is a well-established non-invasive imaging modality, which can be used to complement sonography and detect a variety of pathologies in soft tissues [53, 32, 80] These include tumors in the breast and prostate, thyroid nodules, and skin lesions [53, 32, 80, 31, 26]. In addition to widespread quasi-static elastography techniques, different tissue elasticity imaging methods such as shear wave imaging have been more recently deployed, which can be used in a number of clinical applications ranging from examination of solid breast masses to the detection of liver fibrosis and cervical lymph nodes [22, 23, 7].

While quasi-static elastography methods are currently the most commonly used in clinical applications, in the past few years, additional elastographic techniques have been developed to image the temporal behavior of materials under mechanical loads or stresses [38, 64]. Among these techniques are viscoeleasticity imaging and poroelastography, which have shown potential for in vivo non-invasive diagnosis of breast cancers [57] as well as diagnosis and staging of lymphedema [6, 65]. Viscoelasticity imaging uses elastographic methods to estimate the time-dependent behavior of the axial strains in materials that can be modeled as viscoelastic [45, 68]. Viscoelastic

properties of tissues have been proven to help in the differentiation between malignant and benign tumors [73]. Poroelasticity imaging uses elastographic techniques for imaging the temporal behavior of materials that can be modeled as sponges, that is, consisting of a solid skeleton, or matrix, filled with fluid [2, 4, 61]. In both viscoelastic and poroelastic models of tissues under stress relaxation or creep tests, the strain time constants (TCs) are indicative of the underlying tissue mechanical properties [2, 18, 51]. Consequently, in the past few years, several algorithms have been proposed that deal with the estimation of the local TC from sets of temporal strain data [4, 65, 51, 1].

Previous studies have shown that elastographic TC imaging may be useful for real-time clinical applications [57, 6, 65]. These applications include the characterization of non-palpable breast lesions, [22], the tracking of changes in tissue mechanical properties with lymphedema [6], and the determination of the presence of pathologies based on non-uniformities in tissues [61]. However, the clinical applicability of these techniques is sometimes challenged by the long time required for the acquisition of raw ultrasonic data necessary to generate the TC elastogram [51]. Minimization of this time would be beneficial in clinical applications and for real-time diagnostic imaging. Furthermore, previous work has suggested that the relationship between the acquisition time (of the raw ultrasonic temporal data) and the quality of the resulting elastographic TC estimates depends on the level of noise present in the acquired strain-versus-time curves and also on the elastographic TC for the theoretical, noiseless strain-versus-time curve typical of the sample being tested [51]. *A further investigation of this relationship could significantly improve our basic understanding of elastographic TC methods.*

While studies that deal with elastographic TC estimation (both for viscoelastic and poroelastic tissue models) are retrievable in the literature, the minimum data ac-

quisition requirements necessary to make accurate and reliable strain TC estimations are yet unclear. This problem is challenging as strain TC estimations are typically acquired through least square error (LSE) minimization, which needs careful consideration of sampling requirements that have not yet been fully studied.

This work aims at exploring the data acquisition requirements necessary to make accurate and reliable elastographic TC estimations. More specifically, the effects of window of observation (WoO), acquisition rate, and input noise on TC estimation were studied. With the results of this study, the relationship between the WoO necessary for accurate strain TC estimations and the underlying theoretical TC will be elucidated. The study also investigates the possibility of obtaining accurate TC estimates when using acquisition times significantly smaller than the underlying theoretical TC. This result could have important implications for clinical applications of temporal elastographic techniques. Finally, the effects of input noise and acquisition rate on the accuracy of the resulting strain TC estimates is studied. While the results of the study shown in this chapter specifically refer to ultrasound TC elastography, the findings reported here may be useful for general studies aiming at estimating the temporal mechanical behavior of tissues.

3.2   Methods

3.2.1   Model used for the study

When a viscoelastic or poroelastic tissue is subjected to a constant force or displacement, the strain experienced by the tissue changes with time. The TCs associated with the strain temporal data can be estimated using a number of models, which include exponential polynomials [2, 70, 74].

The study shown in this chapter deals with a simplified single-exponential model suitable for strain temporal tracking in viscoelastic, and under simplified conditions,

in poroelastic material. Based on this model and in the presence of noise, the temporal behavior of strain experienced by a material under compression may be approximated as shown in equation 3.1.

$$s(t_i) = \eta + (\alpha - \eta)e^{-\frac{t_i}{\tau}} + N_i(t_i), t > 0 \tag{3.1}$$

In this equation $s(t_i)$ is a strain sample at time t_i, η is the equilibrium strain at time $t = \infty$, α is the initial strain at time $t = 0^+$, τ is the theoretical strain time constant (TC), and $N_i(t_i)$ is random noise. In equation 3.1, the noise at each sample point $N_i(t_i)$ is assumed to come from a zero-mean Gaussian noise distribution. In viscoelastic materials, $\alpha = 0$. In this study, we use this model with the assumption of a constant signal-to-noise ratio (SNR) for the entire duration of the signal.

The two parameters of interest in this model that are typically unknown are the TC, τ and the equilibrium point (EP) strain value, η. Extraction of these two parameters from a given set of noisy data is typically performed using curve-fitting methods. This chapter focuses on the time requirements for accurate and reliable estimation of τ. Similar considerations can also be applied to η.

3.2.2   Simulations

The simulations followed the model given by equation 3.1. Each simulated curve corresponded to a given value of the strain TC τ while setting the values of α and η at 0.0001 and 0.25, respectively, as used in previous work [51]. The values of τ used in this study varied within the range $5s$ and $300s$, in increments of $5s$. Table 3.1 shows a table describing the cases studied. These values may be representative of the TCs expected in some tissues and tissue-mimicking materials [64, 57, 6]. However, the results of this study can be easily extended to values of TCs outside the range, if needed. The amount of additive noise on the strain estimates was also varied

within the range specified in table 3.1 and as explained below. Fifty independent realizations were considered for each analyzed case.

Table 3.1: Input parameters used for the simulation study

Minimum TC	Maximum TC	SNR (dB)	Acquisition Rate (Hz)	Largest Window of observation (% TC)
5	300	10	100	250
5	300	15	100	250
5	300	20	100	250
5	300	25	100	250
5	300	30	100	250
5	300	30	20	250
5	300	30	2	250

3.2.3   Statistical analysis

As a measure of the quality of the estimator, the following image quality factors were computed. The mean absolute error (MAE) for the estimator was computed for a series of 50 estimates as in equation 3.2.

$$MeanAbsoluteError(\%) = mean(\frac{|\hat{\tau}_i - \tau|}{\tau}) \times 100 \qquad (3.2)$$

In this equation $\hat{\tau}_i$ is the series of 50 estimates acquired from the estimator and τ is the underlying theoretical strain TC. The MAE differs from the previously used measure of percent bias from [51]. While the bias is a measure that is strictly related to the estimator's accuracy, the MAE is a quality factor that is affected by both the accuracy and the precision of the estimator - the lower the MAE, the better the quality of the estimator.

For a given τ, a threshold window of observation (TWO) is defined as the shortest window of observation such that the MAE would be less than or equal 10% so as to guarantee a certain level of quality. The level of quality required is dependent on the application for which TC imaging is being used and, in this case, was chosen arbitrarily. However, the choice of an $MAE \leq 10\%$ is consistent with a previously executed study on breast cancer imaging found in the literature [57]. While, in general, the actual values of the TWO may be different if a different threshold is chosen, its functionality and the overall qualitative analysis reported below do not depend on the chosen threshold. The TWO can be expressed in seconds or as a percentage of the theoretical TC as in equation 3.3.

$$TWO(\%TC) = \frac{total\,acquisition\,time}{\tau} \times 100 \qquad (3.3)$$

Measuring the TWO in seconds is useful because it gives a simple and potentially practical estimate of the time necessary to accurately estimate a strain TC under a specific set of acquisition parameters. Measuring the TWO in terms of percentage of the theoretical TC is useful for theoretical analysis even though, in practice, the underlying TC of a material is often unknown. The usefulness of this theoretical analysis comes from the fact that it is well understood that the range of TCs that can be expected for a given tissue are application dependent and can be studied in the future.

To determine the TWO corresponding to a given TC, the MAE was computed for each simulated curve while the WoO was varied in increments of 1% of the underlying theoretical TC. The last analyzed WoO corresponded to 250% of the TC. This value was found to be sufficient for the analysis in all cases.

The effect on the TWO by other acquisition parameters, such as acquisition rate

and input SNR, was also analyzed by running multiple simulations with varying acquisition rates and input SNR over the same range of TCs (see Table 3.1).

The final parameter considered for the statistical analysis was the output SNR of the TC estimator which can be calculated as in equation 3.4.

$$SNR = 20log_{10}(\frac{mean(\hat{\tau}_i)}{std(t\hat{a}u_i)}) \tag{3.4}$$

3.2.4 Experiments

Simulation data typically provide upper bound performance assessment because they cannot take into consideration all possible factors that may influence experimental results. Therefore, a set of experiments with the goal of corroborating the simulation results in specific testing conditions was performed. The set of experiments was performed using a phantom material previously used for elastographic TC experiments [51, 85]. The sample was placed in a water tank and compressed from the top using an apparatus that applied a constant compressive force to the sample. Ultrasound radio frequency (RF) data were acquired using a $38mm$ real-time linear array scanner Sonix RB(Ultrasonix, Richmond, British Colombia, Canada) that has 128 elements, a bandwidth between 5 and 14 MHz, a center frequency of $6.6MHz$, 50% fractional bandwidth at $-6dB$, sampling frequency of $40MHz$ and $1mm$ beam width at the focus. The data were acquired for $600s$ at an average frame rate of 1 $frame/s$ while the sample was subjected to creep compression. This choice of WoO and frame rate was dictated by memory limitations of the buffer in the ultrasound system available at the time in the TAMU ultrasound lab. It has been proven to be sufficient for accurate strain TC measurements in the type of phantom used for this study [51]. Temporal axial strain elastograms were generated from the time-series of RF data using cross-correlation techniques, and axial strain TC elastograms were

26

generated from the temporal axial strain elastograms using an LM LSE minimization algorithm [51].

The effect of the WoO on the experimental strain TC estimation was evaluated in the following manner. First, a base axial strain TC elastogram of the phantom being tested was obtained using all temporal data $(0 - 800s)$. To analyze the effect of WoO reduction, the WoO was reduced by truncating the temporal data. For each WoO analyzed, a new axial strain TC elastogram was computed. The MAE was evaluated as specified in equation 3.2, with $\hat{\tau}_i$ estimated from the new axial axial strain TC elastogram and τ set equal to the mean axial strain TC estimated from the elastogram corresponding to the largest WoO. Although this value may not be strictly equal to the true underlying axial strain TC, a previous study has shown that it is close to the true underlying average strain TC (measured through mechanical testing) within $\pm 10\%$ [64, 51]. The experimental data were statistically compared with corresponding simulations.

3.3 Results

3.3.1 Simulation results

Figure 3.1 shows the MAE for the strain TC estimator as a function of the WoO for five different values of underlying theoretical strain TC. Statistical analysis of the simulation data reported in figure 3.1 is between 15% to 20% of the theoretical TC for most TC curves analyzed in this study. This threshold is significantly higher for the $5s$ TC (presumably due to the fact that, for these small TC values, the estimator does not have a sufficient number of data points to produce an error-less TC estimate).

Figures 3.2 and 3.3 show the effect of input strain SNR on the TWO for TCs ranging between $5s$ and $300s$. As the input noise increases, the estimator requires a
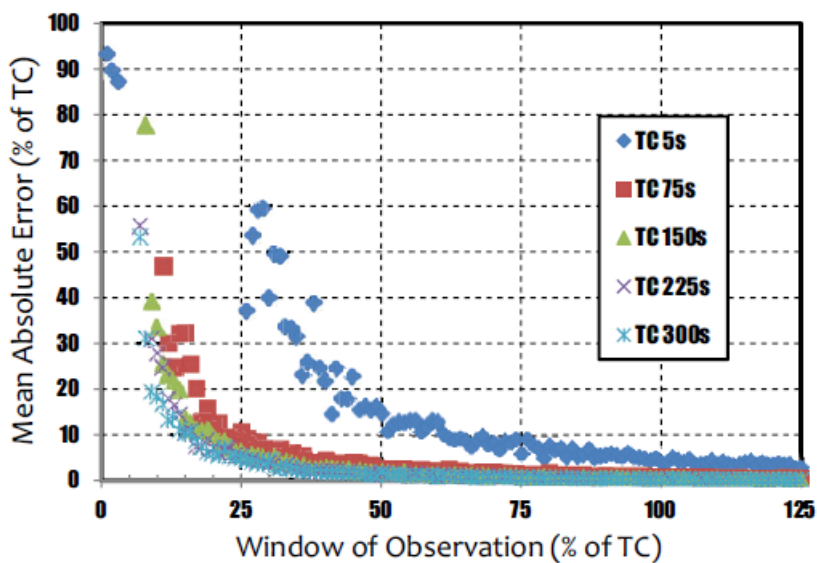
Figure 3.1: MAE for the TC estimator as a function of the WoO for different time constants when the strain $SNR = 20dB$ and the strain sampling frequency is $100Hz$

longer TWO to compute more correct TC estimates, especially for small TC values. Clearly, strain input noise plays a significant role in the performance of the TC estimator.

Figures 3.4 and 3.5 show the effect of acquisition rate on the TWO for TCs ranging between $5s$ and $300s$. These figures suggest that the acquisition rate can have a significant impact on the amount of time necessary that allows high performance TC estimation. Note that Figures 3.3 and 3.5 give a direct relationship between the total acquisition time required for quality TC estimation and the underlying theoretical TC. These results suggest that there is a linear relationship between the TWO and the underlying theoretical TC. The linear regression fits of the data in these two figures reveal coefficients of determinations R^2 consistently greater than 0.9. The slope of the line describing this relationship depends not only on the input SNR but also on the acquisition rate being used.

28
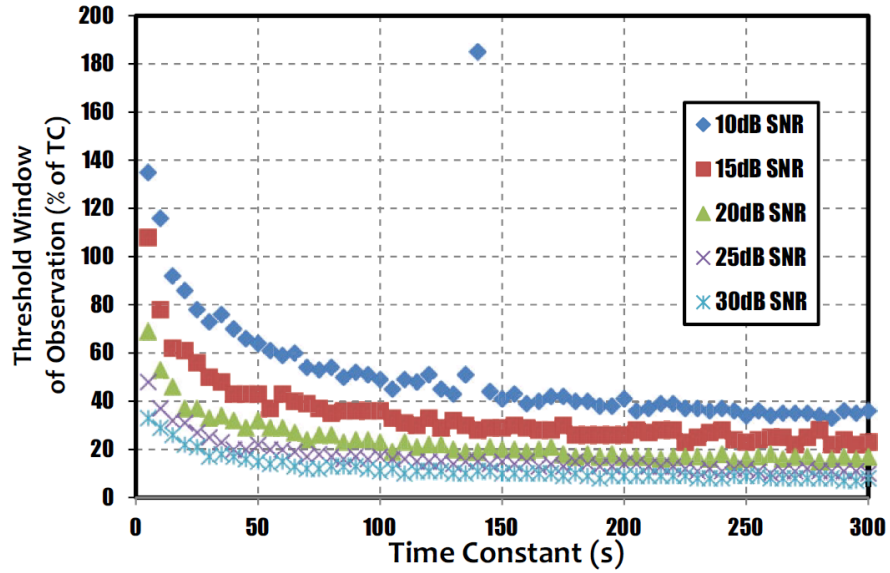
Figure 3.2: TWO expressed as a percentage of the underlying theoretical TC for different values of input strain SNR at a $100Hz$ strain sampling frequency
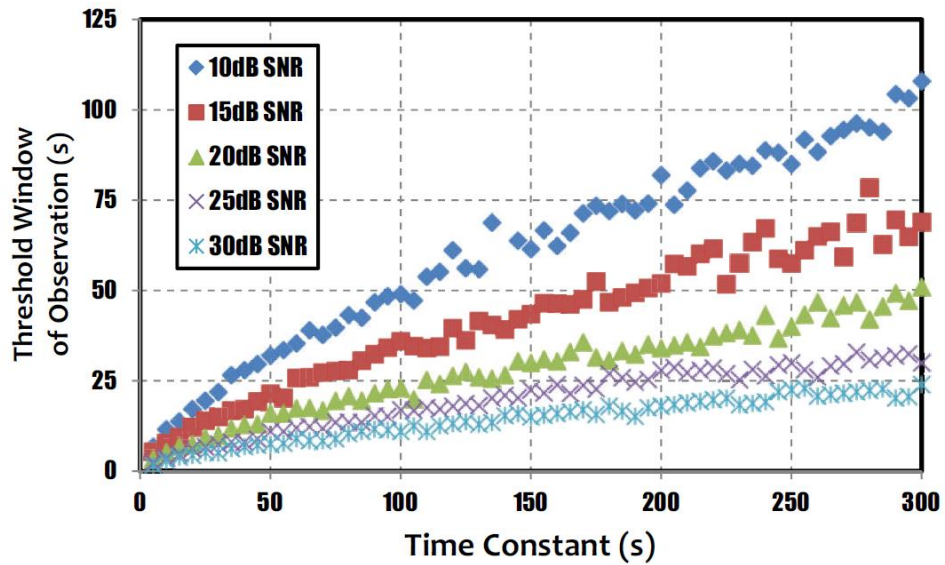
Figure 3.3: TWO expressed in seconds for different values of input strain SNR at a $100Hz$ strain sampling frequency
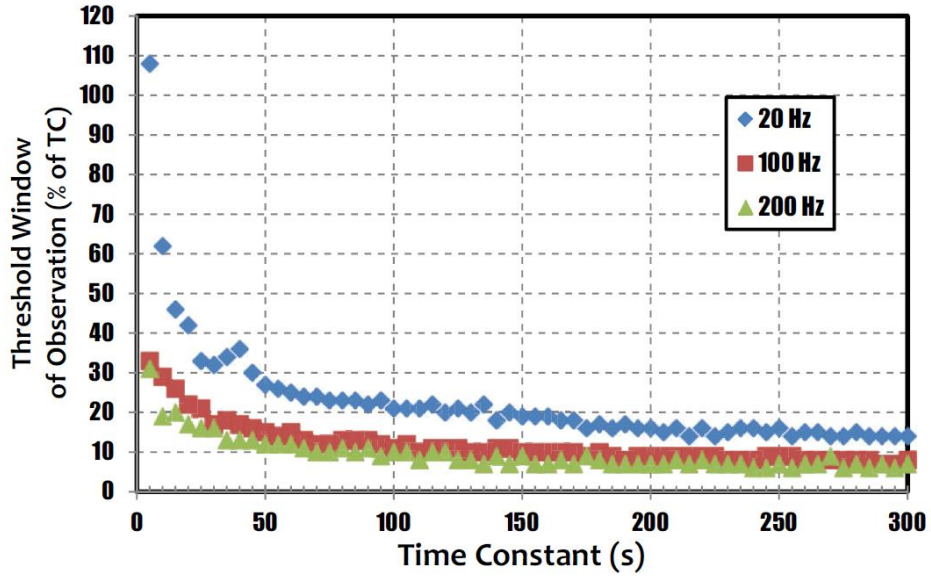
Figure 3.4: TWO expressed as a percentage of the underlying theoretical as a function of the theoretical TC for different acquisition rates when the strain $SNR = 30dB$.
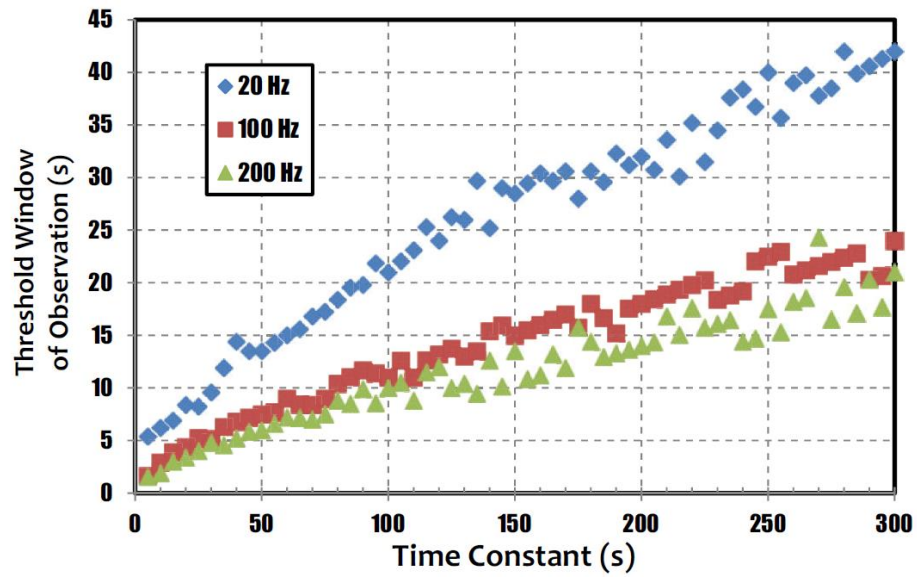
Figure 3.5: TWO expressed in seconds as a function of the theoretical TC for different acquisition rates when the strain $SNR = 30dB$.

30
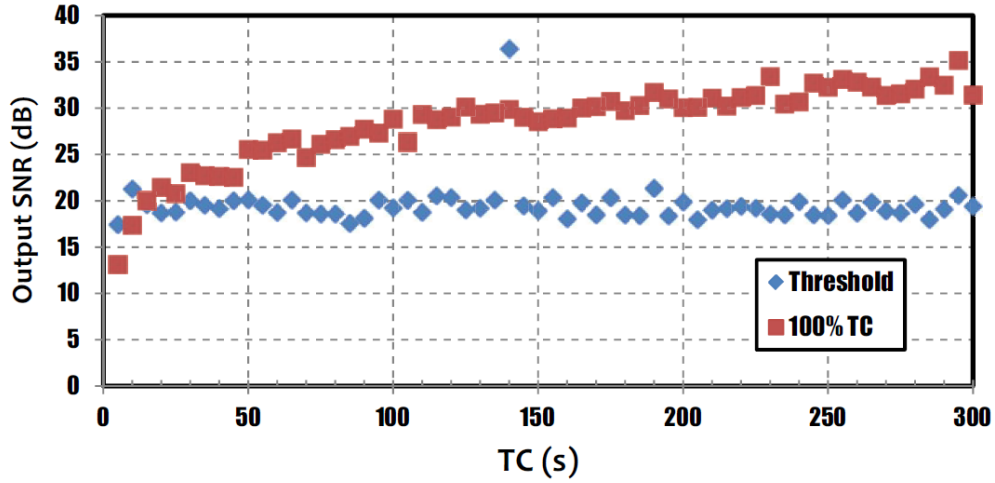
Figure 3.6: Expected output SNR of the TC estimator as a function of the theoretical TC when the input strain $SNR = 10dB$ and the strain sampling rate is $100Hz$

Figures 3.6, 3.7 and 3.8 show the expected output SNR of the TC estimator as a function of TC for an input strain SNR of $10dB$, $20dB$, and $30dB$ respectively. In each of these figures, the output SNR obtained when using a WoO equal to the TWO is compared with the output SNR for a WoO equal to 100% of the theoretical TC. As it can be observed from these graphs, the output SNR of the TC estimator obtained when using a WoO equal to 100% of the theoretical TC can be significantly higher than the output SNR obtained when using the TWO. However, use of the TWO guarantees at least a certain level of output SNR, regardless of the input SNR - in our case, approximately $20dB$. This specific value is a result of the way the TWO was defined in this study. This result is consistent with previous findings [51].

Figure 3.9 shows the expected output SNR of the TC estimator as a function of the sampling period in logarithmic scale for three values of input strain SNR. For these simulations, the underlying theoretical strain TC was fixed at 100 s and

31
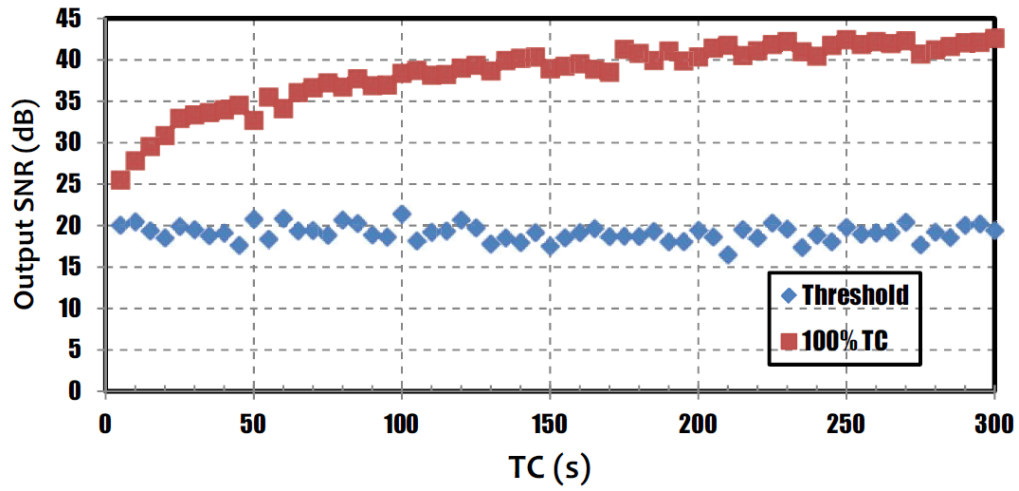
Figure 3.7: Expected output SNR of the TC estimator as a function of the theoretical TC when the input strain $SNR = 20dB$ and the strain sampling rate is $100Hz$
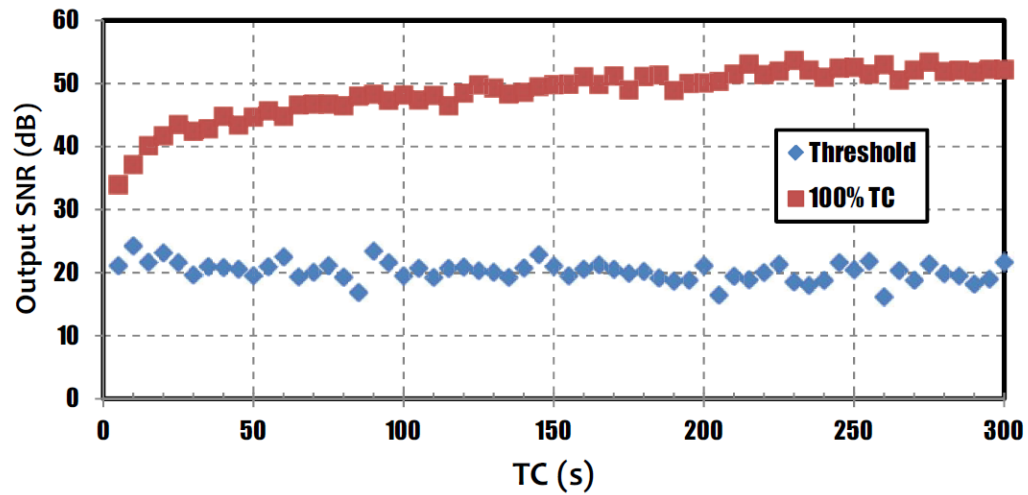
Figure 3.8: Expected output SNR of the TC estimator as a function of the theoretical TC when the input strain $SNR = 30dB$ and the strain sampling rate is $100Hz$
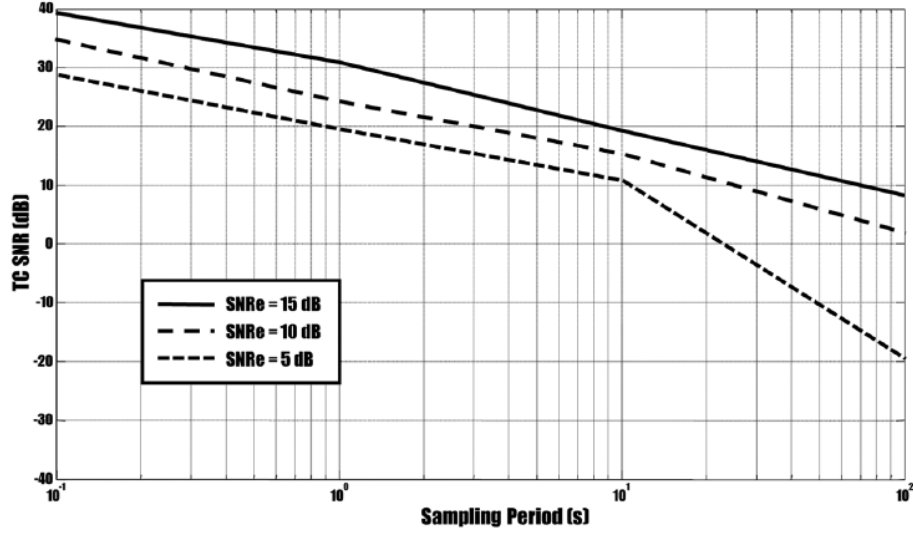
Figure 3.9: Expected output SNR of the TC estimator as a function of the sampling period for different input strain SNRs. The theoretical $TC = 100s$ and WoO is fixed at $100s$.

the WoO at 100 s. This figure shows that the TC SNR decreases exponentially as the sampling period increases. Note that, provided that the sampling period is sufficiently short, the output SNR of the TC estimator is in general higher than the input strain SNR. These output SNR results can be intuitively explained by the fact that the LSE curve-fitting estimation behaves as a filter on the strain samples as it was also observed in an earlier study [51].

3.3.2   Experimental results

Figure 3.10 (top) shows an experimental axial strain TC elastogram obtained form the poroelastic phantom subjected to creep compression. The axial strain TC elastogram was computed using all acquired temporal data (0 - 600s) and was used as reference for the MAE computation. The top figure shows a selected area where the mean axial strain $TC = 142s \pm 24s$ and the elastographic $SNR = 14.38dB$. The
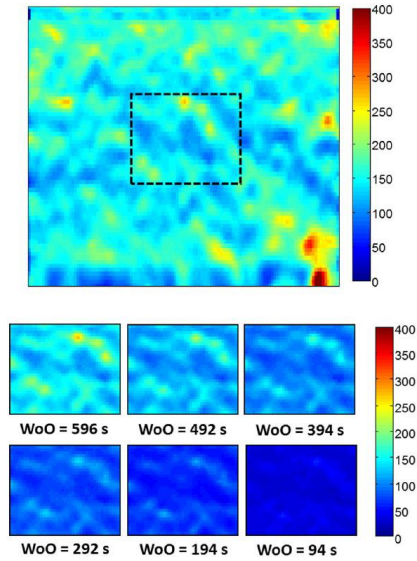
Figure 3.10: Experimental axial strain TC elastograms obtained from a phantom under creep compression

series of images at the bottom of figure 3.10 represent axial strain TC elastograms (of the selected area) obtained using reduced WoOs.

In figure 3.10 the use of shorter WoOs generally leads to an underestimation of the axial strain TC. This is intuitive, as higher TC curves display more unique information at higher times. This unique information is lost when a lower WoO is chosen. Thus, a higher TC curve may behave as a lower TC curve within a relatively short WoO, and the high TC values may be incorrectly estimated as low TC values because there is simply insufficient time for the curve to manifest its real TC. This may result in more uniform TC images with overall underestimated TC values. This could explain why the output SNR of the experimental TC elastograms does not seem to be visibly deteriorated (and, in fact, seems to improve) by the use of a reduced WoO. Thus, it is evident that observation of a TC image's SNR may not constitute a reliable measure of TC estimation correctness.
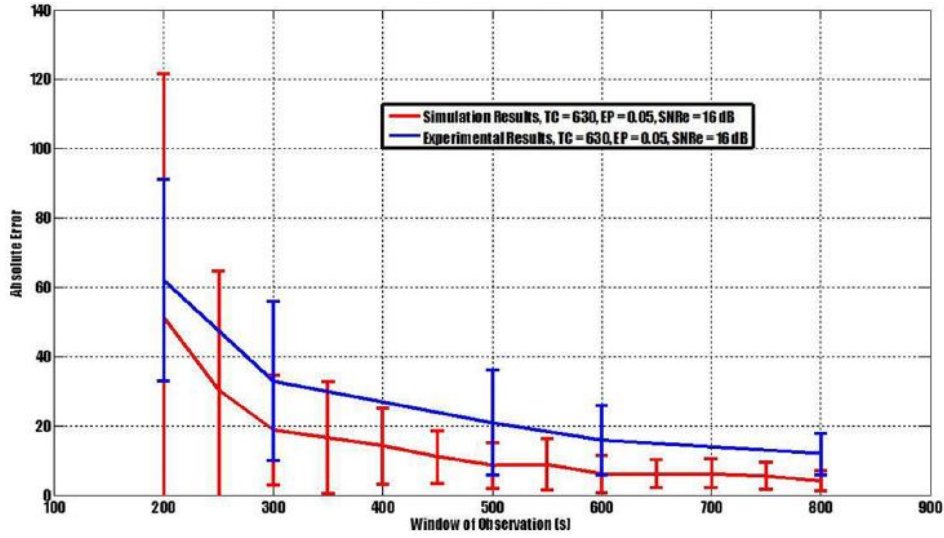
Figure 3.11: Experimental MAE and predicted MAE as a function of WoO

Figure 3.11 shows the MAE obtained from the experimental data (blue line). For comparison, the MAE obtained using the corresponding simulation data is also reported (red line). Analysis of the experimental results shows a statistical equivalence between the experimental MAE and the MAE predicted by the simulations. Thus, the simulation results may be used as upper bound guidance for the prediction of the acquisition parameters to be used in a given TC estimation experiment. However, Figure 3.11 can be acquired in experiments at about 1.5 to 2 times the WoO that is predicted in simulations. This factor may be higher if dealing with very low elastographic SNR or may be lower for very high acquisition frame rates.

3.4   Discussion

This chapter investigated the effects of temporal acquisition parameters on elastographic TC estimation. Using a simulation model, it shows that the error associated with estimating a strain TC depends on the temporal WoO used. The simulation

35

results reported in this chapter show that both the input strain SNR and the acquisition rate may have a significant impact on the window of acquisition for error-less TC estimations. Consequently, the quality of the resulting TC estimates may be directly related to the relative weights of these two parameters. For example, it may be possible to obtain TC estimates with a predefined level of quality even with relatively short WoO (compared with the underlying TC) provided sufficiently high acquisition rates. This is an important observation, which may have implications not only for current ultrasound elastographic techniques but also for other imaging modalities dealing with exponential TC estimation. For example, the development of ultrafast magnetic resonance (MR) elastography systems may prove to be beneficial for studies aiming at imagin time-dependent phenomena in tissue [11]. However, increased acquisition rates affect the TWO (and consequently the quality of the TC estimation) only up to a certain point. For example, figures 3.4 and 3.5 do not show any statistcally significant reduction the TWO by increasing the acquisition rate from $100Hz$ to $200Hz$. Similarly, increased input strain SNR values result in shorter required TWOs. As for the acquisition rate case, the results obtained with different input strain SNR values (Figures 3.2 and 3.3) seem to suggest that the effect of this parameter on the required WoO exhibit an asymptotic behavior. Thus, the use of high-quality strain estimators is suggested in real-time, clinical applications. On the contrary, when dealing with inherently noisy estimator, such as those that require lateral strain estimation [38, 61], it may be necessary to use higher WoOs to guarantee at least a certain level of output SNR.

The results of this study also suggest the presence of a linear relationship between the WoO necessary for error-less TC estimation and the underlying theoretical TC. This result might be useful to predict the required data acquisition parameters in a given clinical application. Ideally, the findings of this study could be translated into

a simple tool that could be used by a physician or ultrasound technician to quickly and automatically determine the window of acquisition of ultrasound data in a given clinical elastography application. Creation of a database with the expected strain TCs corresponding to various tissues, such as tumors, muscles, and other soft tissues, would be the first step towards this goal.

This chapter also presented a pilot experimental study, which shows the beginnings of an experimental methodology that my be used in the future to fully statistically corroborate the simulation analysis presented. The limited experimental results reported in this study suggest that simulation data may be used as an upper predictor bound of the acquisition parameters for strain TC estimation, possibly providing useful and practical guidance in the design of TC elastography experiments [53, 76].

The use of extended WoOs may pose severe limitations on the applicability of elastographic TC techniques in clinical settings. While the use of long WoOs is often benefitial for the quality of the resulting TC elastograms, in clinical applications, it might be possible to reduce the acquisition window and still maintain the same level of image quality by increasing the acquisition rate. Typical ultrasound systems have a limited buffer for acquiring samples. In addition, physics imposes limitation on the highest rate that can be used to acquire ultrasonic data, which depends on the depth of the tissue being imaged. This limitation may not exist in other imaging modalities. This study shows that until the limits imposed by physics and data buffer are reached, quality elastographic TC estimation becomes a matter of properly tuning the acquisition rate and the WoO to the range of the TCs expected from the tissue being investigated.

The work presented in this chapter might be a starting point for the development of a more general theoretical framework describing the SNR for strain TC imaging as a function of sampling frequency, WoO, underlying TC, and input strain SNR. This

article has shown that the solution of such a sampling problem is challenging as it requires in-depth exploration of non-linear LSE parameter estimation. While, indeed, LSE parameter estimation is itself easily implementable, as there are several software packages that are readily available, its theoretical intricacies and complications are often erroneously overlooked.

While the scope of this work was limited to the study of the effects of selected acquisition parameters on strain TC estimation, the findings of this work may be more generally applicable to the estimation of other time-dependent elastographic parameters and also for elastographic techniques other than ultrasound elastography, such as MR elastography. Even more generally, the results shown in this work may be valuable for studies outside the field of elastography that involve exponential TC estimation.

3.5   Conclusion

This chapter investigated the temporal acquisition parameters on strain TC estimation. The study shows that the total acquisition time necessary for error-less TC estimates depends on the underlying TC values. The results also show that error-less estimates of the strain TC could be achieved with WoO significantly shorter than the underlying theoretical TC provided fast acquisition rates. These results may have practical implication in studies that aim at imaging the temporal behavior of tissues.

It should be noted that this study also brings up an interesting doubt. The experimental study shows that despite the fact that the TC estimator was more incorrect when the experimental window of observation decreased, that the image SNR increased. In medical imaging, judgment on the correctness of the image is often based on how noisy or visually appealing the image appears to be. However, the study shows that this is perhaps incorrect.

38

Now that a full understanding of the sampling requirements of the TC estimator has been acquired, it's important to develop a measurement of how well the curve estimated by the LM LSE method fits a given set of data. The next chapter of this dissertation tackles that problem.

4. RESIMULATION OF NOISE: A PRECISION ESTIMATOR FOR LEAST
SQUARE ERROR CURVE-FITTING TESTED FOR AXIAL STRAIN TIME
CONSTANT IMAGING*

Devising a measurement of how reliably a TC curve fits a set of temporal strain
data is one of the key elements of this dissertation. About 2 years were spent devising
and formalizing an algorithm that could show an easily understandable measurement
of reliability. While the algorithm was only tested and implemented for single expo-
nential time constant curve-fitting, it is likely that it can be used for all non-linear
least square error curve-fitting. The work shown in this chapter was published as a
peer-reviewed journal article [49], which as of this writing, received the best praise
from reviewers in my career.

4.1   Introduction

Ultrasound elastography is a well-established non-invasive imaging modality, which
can be used to complement ultrasound B-mode imaging to aid in the diagnosis and
staging of various diseases and pathologies in soft tissues [53, 32, 80, 81]. Elastog-
raphy images the local strains that tissues undergo when placed under a mechanical
stress or load resulting in what are referred to as 'strain elastograms'. Axial strain
elastograms are images of the strain tensor component along the axis of insonifica-
tion [51]. These have been shown to be highly correlated with changes in the tissue
stiffness distribution when the tissue is assumed to behave as a linearly elastic solid
[75].

Most clinical elastography methods implement a quasi-static stress to image time

40

independent strain behavior of tissues. However, in the past several years, novel emerging elastographic techniques have been proposed that may allow imaging additional mechanical properties of tissues related to the tissue's temporal behavior. Several mathematical models and imaging techniques have been used to study the time dependent behavior of tissues under mechanical loads.

Poroelastography refers to the application of elastography techniques for imaging the temporal behaviour of materials that can be modeled as poroelastic media, due to their relative high fluid content and mobility [38, 63, 64, 4, 5, 56]. A poroelastic material is typically modeled as consisting of a solid matrix filled with a fluid [2, 4, 5, 61]. Similarly, viscoelasticity imaging refers to the application of elastography techniques for imaging the temporal behavior of materials that can be modeled as viscoelastic media [68, 45, 74]. A viscoelastic material can be modeled as a spring and dashpot system. Viscoelastic properties of tissues have been shown to correlate well with pathological changes in stroma and connective tissues [73].

These novel temporal elastographic modalities have led to the creation of several types of elastograms that may provide new information about the behavior of tissues. Among these are the effective Poisson's ratio (EPR) elastogram, the poroelastogram, the time constant (TC) elastogram, the axial strain equilibrium point (EP) elastogram, and the EPR TC elastogram. For clarification, it's worth mentioning that for both poroelastic and viscoelastic media, the strain response due to creep compression and stress relaxation follow an exponential saturating pattern with a time constant and equilibrium point similar to the step response of an RC circuit [51]. Axial strain TC and EP elastograms are images of the time constants and equilibrium points calculated pixel by pixel from a collection of axial axial strain elastograms [51]. Technical details on TC and EP elastograms as well as EPR elastograms can be found in previously published work [38, 61, 51, 50, 14]. Several

of these elastograms are generated by using Least Square Error (LSE) parameter estimation with a root-finding algorithm such as the Levenberg-Marquardt (LM) method. The global objective of this chapter is to provide a measure of reliability for the estimated parameters.

LSE estimation can be applied for both viscoelastic and poroelastic tissues [61, 51, 1, 50, 14]. In the viscoelastic case, the TC is a function of both the stiffness and viscosity of the tissue. In the poroelastic case, the TC is a function of the stiffness and permeability of the solid matrix and the viscosity of the fluid matrix [2, 14]. Nair et al [51] presented and analyzed a real-time Levenberg-Marquardt (LM) optimized least square error (LSE) based estimator implemented on a graphics processing unit (GPU). In [50] that analysis was extended to present an assessment of LM and EP estimation correctness that can be expected for a given strain signal to noise ratio (SNR), strain sampling rate, and strain window of observation.

Several works have dealt with elastographic TC estimations, some even proposing the use of TC estimation for diagnostic purposes [51, 50, 57]. Nair et al [51, 50] have referenced the need for an easily understandable measure of reliability of TC and EP estimates. The literature surveyed so far has made no serious effort to tackle the problem of estimate reliability measurement. Available literature has done extensive studies which suggest that the quality of strain TC estimates can be assessed by observing image quality measures - like image SNR and CNR- of the resulting TC and EP images. However, these image quality measures can result in a false assessment of estimated quality. In clinical situations, a measure of estimated reliability would be of utmost importance as the images used for immediate diagnosis may seem usable and yet be completely incorrect.

In LSE estimation, a typical measure of reliability that is used is the correlation coefficient (CorrCoef) between experimental data points available and the resulting

estimated curve [29]. This CorrCoef between two populations is the covariance between the populations divided by the product of each population's standard deviation. This measure is suitable when the data points are fit to a linear model, as the CorrCoef provides a measure of the linearity of the relationship between two sets of data. When the model fitted to is not linear - as is the case with strain TC imaging as well as in other imaging modalities [46]- the CorrCoef can provide a measure of overlap between the estimated curve and the data points being fitted as a complete overlap will result in CorrCoef =1. However, it does not address failures of reliability that can come from data sampling conditions which have been found to be crucial for correct TC estimation [50].

Specifically, the work in this chapter analyzes a novel technique for estimating the precision of LSE estimates called Resimulation of Noise (RoN) and tests it for the estimation of axial strain TC estimates. This algorithm presents a reliability measure for both TC estimates in terms of the spread of these estimates, under the same data acquisition conditions. The RoN algorithm presents this in an easy to understand $\pm Error$ format. While the RoN algorithm was implemented specifically for ultrasound elastographic TC and EP estimation, the algorithm can be easily modified and made useful for other imaging and parameter estimation beyond ultrasound and imaging applications.

4.2 Theoretical background

4.2.1 Least square error parameter estimation and the general RoN algorithm

Least Square Error (LSE) parameter estimation of time dependent phenomena aims to fit a series of n samples in time, $s(t_i)$, that have been affected by additive Gaussian noise, to a model (function), $f(X, t)$, where X is the set of parameters for function f. LSE estimation is well-suited for ultrasound elastography applications

as the noise affecting strain measurements is often modeled as Gaussian [14, 83]. LSE finds the best fit by finding $\hat{X}$ that minimizes the square error (SE) between $s(t_i)$ and $f(X, t)$. The square error is defined by Equation 4.1

$$SE(\hat{X}) = \sum_{i=1}^{n} (s(t_i) - f(\hat{X}, t_i))^2 \qquad (4.1)$$

Resimulation of noise creates a series of noisy samples from the original samples and the estimated curve with the following resimulation algorithm:

1. From the original $s(t_i)$, estimate parameters $\hat{X}$ using LSE LM.

2. For each $s(t_i)$ calculate $d^2(t_i) = (s(t_i) - f(\hat{X}, t_i))^2$.

3. Simulate a series $\tilde{s}_j(t_i) = f(\hat{X}, t_i) + N(0, d(t_i))$ for $1 \le j \le r$ where r is the desired number of resimulation trials and $N(0, d(t_i))$ is a sampling from Gaussian random variable that is zero-mean and with standard deviation $d(t_i)$.

4. For each series $\tilde{s}_j(t_i)$ estimate $(\tilde{X}_j)$ using LSE LM

5. Calculate $\sigma_{\tilde{X}} = stddev(\tilde{X}_j)$

The resimulation of noise algorithm artificially creates a series of 'resamplings' of $s(t_i)$. Typically, it would be preferable to resample $s(t_i)$ by performing a retrial of an experiment under the exact same conditions, but this can often be impossible.

However, assuming an n number of experiment trials were indeed possible, each providing an estimate $\hat{X}_k$, then a good measure of reliability given a particular level of noise would be to find the standard deviations $\sigma_{\hat{X}} = stddev(\hat{X}_k)$. $\sigma_{\hat{X}}$ would give a measure of how much variability can be expected in the estimate. The RoN method tries to simulate the process of creating several experiment trials. Ideally, for the resimulation method $\sigma_{\tilde{X}} \approx \sigma_{\hat{X}}$.

For poroelasticity and viscoelasticity TC imaging, a common and useful simplified approximation of the temporal behavior of an elastographic parameter of interest s is given by Equation 4.2 [51, 57, 2, 61, 50]

$$s(t) = \eta + (\alpha - \eta)e^{-\frac{t}{\tau}} \tag{4.2}$$

where $s(t)$ is the value of the elastographic parameter of interest at time t, α is the value of s at time $t = 0^+$ (i.e., immediately after the application of the excitation), η is the equilibrium point (E.P) (i.e. $s(t)$, at $t = \infty$) of the elastographic parameter of interest and τ is the time constant (TC) of the elastographic parameter of interest.

Thus, the acquirable noisy samples of the strain s, denoted $s(t_i)$, are given by Equation 4.3 [51, 50].

$$s(t_i) = \eta + (\alpha - \eta)e^{-\frac{t_i}{\tau}} + N_i(t_i), 1 \leq i \leq m \tag{4.3}$$

where $s(t_i)$ is the sample at time t_i and $N_i(t_i)$ is the noise level at time t_i. In this mathematical model each $N_i(t_i)$ is assumed to come from a zero-mean Gaussian noise distribution (i.e., $N_i(t_i) \sim N(0, \sigma_i)$) [51, 30, 76]. Because in elastography applications $t_1 \approx 0$ and the noise level in $s(t_1)$ is low α does not need to be estimated using the LSE method and can instead be estimated as $\alpha \approx s(t_1)$ [51]. Therefore, the LSE equation becomes:

$$LSE(\hat{\tau}, \hat{\eta}) = \sum_{i=1}^{n}(s(t_i) - (\hat{\eta} + (\alpha - \hat{\eta})e^{-\frac{-t_i}{\hat{\tau}}}))^2 \tag{4.4}$$

This chapter will test the RoN LSE estimate precision estimator for the time constant model shown in Equation 4.2, specifically for s being the axial strain. For

clarity, the RoN algorithm is specified for the axial strain TC case as follows:

1. From the original $s(t_i)$, estimate $(\hat{\tau}, \hat{\eta})$ using LSE LM.

2. For each $s(t_i)$ calculate $d^2(t_i) = (s(t_i) - (\hat{\eta} + (\alpha - \hat{\eta})e^{-\frac{t_i}{\hat{\tau}}}))^2$.

3. Simulate a series $\tilde{s}_j(t_i) = \hat{\eta} + (\alpha - \hat{\eta})e^{-\frac{t_i}{\hat{\tau}}} + N(0, d(t_i))$ for $1 \leq j \leq r$ where r is the desired number of resimulation trials.

4. For a particular series $\tilde{s}_j(t_i)$ estimate $(\tilde{\tau}_j, \tilde{\eta}_j)$ using LSE LM

5. Calculate $\sigma_{\tilde{\tau}} = stddev(\tilde{\tau}_j)$ and $\sigma_{\tilde{\eta}} = stddev(\tilde{\eta}_j)$

4.3   Methods

4.3.1   Noise model

The noise model used during simulations is additive Gaussian distribution noise with a constant elastogram SNR. This noise model has been used previously and is consistent with the nature of temporal elastography experiments [51]. SNR for a strain sample $s(t_i)$ curve, is calculated as $SNR(dB) = 20 \times \log mean(s(t_i))/stddev(s(t_i))$.

4.3.2   1D simulations

Simulations were carried out to test the veracity of the statement: $\sigma_{\tilde{\tau}} \approx \sigma_{\hat{\tau}}$. $\sigma_{\hat{\eta}} \approx \sigma_{\tilde{\eta}}$ was tested but its results are not shown because prior work has shown that $\hat{\eta}$ estimates are already very reliable, thereby making its analysis uninteresting [50]. All simulations created noisy sampled TC curves as per Equation 4.3 with time samples ranging from 1 s to 600 s and sampled every second. The strain SNRs for this study ranged from 10 dB to 15 dB at increments of 1 dB. The algorithm was tested for sufficiently sampled conditions, where the time constants, τ, were within the range of good LSE estimation for the 1 s strain sampling rate and 600 s window

46

of observation and also for insufficiently conditions, where the time constants were too high to provide a good estimate.

4.3.2.1 Insufficiently sampled and sufficiently sampled conditions

The effectiveness of the LM LSE algorithm for different input strain SNRs, η, and τ has been previously studied and it was shown that the required window of observation (WoO) for near error-less TC estimation is monotonically increasing with respect to τ [50]. The required window of observation was referred to as the threshold window of observation (TWO). To test the resimulation of noise algorithm, two families of cases were studied: one in which the WoO was larger than the TWO (i.e. sufficiently sampled) and another in which the WoO is smaller than the required TWO (i.e. insufficiently sampled) as found in [50]. Since the simulated noisy TC curves are sampled until a time t = 600 s, WoO = 600 s. This is an adequate WoO for TCs less than 1200 s [50]. In order to test how the resimulation of noise algorithm worked for sufficiently sampled conditions, axial strain time constant curves were created with τ within the range of 200 s to 700 s at increments of 50 s and η ranging from 0.05 to 0.15 at increments of 0.01. For insufficiently sampled conditions, axial strain time constant curves were created with τ in the range of 7000 s to 13000 s at increments of 1000 s, and again with η ranging from 0.05 to 0.15 at increments of 0.01.

4.3.2.2 Simulation procedure

For both sufficiently sampled and insufficiently sampled conditions, the RoN spread estimator was compared to the spread of the LM LSE time constant estimator. For a given underlying τ and η, this was done by first creating a theoretical time constant curve $s(t)$, as in Equation 4.2 with time constant τ and η. To calculate the spread of the LM LSE estimator, 100 independent noisy time constant curves

47

$s_k(t_i)$, as in Equation 4.3, were created with k ranging from 1 to 100. The noise added to these samples followed the constant SNR with respect to the noise model mentioned in subsection 4.3.1. Each series $s_k(t_i)$ was then input to the LM LSE estimator, each yielding an estimate $\hat{\tau}_k$. The 100 estimates were used to calculate $\sigma_{\hat{\tau}}$. The first series, $s_1(t_i)$ was input into the resimulation of noise algorithm to generate the spread estimate, $\sigma_{\tilde{\tau}}$. For the purpose of analysis, the percent spread was used and evaluated as:

$$\%\sigma_{\hat{\tau}} = \%spread(\hat{\tau}) = 100 \times \sigma_{\hat{\tau}}/\tau \tag{4.5}$$

$$\%\sigma_{\tilde{\tau}} = \%spread(\tilde{\tau}) = 100 \times \sigma_{\tilde{\tau}}/\tau \tag{4.6}$$

To study the performance of the RoN method as the number of resimulation trials changes, a case where $\tau = 300s$ and $\eta = 0.1$ with strain samples ranging from 1s to 600s taken every second was chosen. The RoN algorithm performance was observed for ranges of $r = 10$ to $r = 100$ at increments of 10. For each, r, 100 trials were executed.

4.3.2.3 Experiments

To show the feasibility of using the RoN method in actual data, an experiment using tofu, a phantom material previously used for elastographic TC experiments [51] was performed. The sample was placed in a water tank, and compressed from the top using an apparatus that applied a constant compressive force to the sample (to perform a creep test). Ultrasound RF data were acquired using a commercially available linear array scanner Sonix RP (Ultrasonix, Richmond, BC, Canada) that has 128 elements, is 38 mm wide, has a bandwidth between 5-14 MHz, a center

frequency of 6.6 MHz, 50% fractional bandwidth at -6 dB, sampling frequency of 40 MHz, and 1 mm beam-width at the focus. The data were acquired for 584 s at an average frame rate of 1 frame/sec while the sample was subjected to creep compression. This choice of window of observation and frame rate was dictated by memory limitations of the buffer in our ultrasound system but has been proven to be sufficient for accurate strain TC measurements in the type of phantom used for this study [51, 50]. Temporal axial strain elastograms were generated from the time-series of RF data using cross-correlation techniques, and axial strain TC elastograms were generated considering data from time = 0 to time = WoO. The WoO that were considered were WoO = {584, 484, 384, 284, 182, 84} s.

For each WoO, three reliability measures were compared for the TC images for each WoO: the SNR of the TC image, the CorrCoef of the estimated TCs of the image, and the estimate of the percent precision of the TC estimates using the RoN method. Intuitively, and also as mentioned in [50], a higher WoO should lead to more reliable TC estimates.

4.4 Results

4.4.1 Simulation results

The results reported here are presented in terms of the average of the percent spreads as shown in Equations 4.5 and 4.6 of all τ and η tested for a particular level of SNR. The average of the the percent spreads $\%\sigma_{\hat{\tau}}$, $\%\sigma_{\tilde{\tau}}$, shall be denoted $\bar{\%}\sigma_{\hat{\tau}}$ and $\bar{\%}\sigma_{\tilde{\tau}}$ respectively.

4.4.1.1 Correctness in sufficiently sampled conditions

Figures 4.1, 4.2 and 4.3, show an analysis of the RoN algorithm for sufficiently sampled conditions as described in section 4.3.2.1. Figure 4.1 shows this analysis when the RoN algorithm has been set for 100 iterations, $r = 100$. Figure 4.2 shows

Figure 4.1: $\bar{\%}\sigma_{\hat{\tau}}$ and $\bar{\%}\sigma_{\tilde{\tau}}$ in sufficiently sampled conditions with RoN iterations $r = 100$.

the average estimated percent spread using the RoN method compared to the LM percent spread for this scenario and shows a near one-to-one relationship between the RoN estimated precision and the precision of the LM algorithm. Figure 4.3 shows the average correlation coefficient of the estimated TC curves using LM and the original noisy curve.

4.4.1.2   Correctness in insufficiently sampled conditions

Figures 4.4, 4.5, and 4.6, show an analysis of the RoN algorithm under insufficiently sampled conditions as described in section 4.3.2.1. Figure 4.4 shows this analysis when the RoN algorithm has been set for $r = 100$ resimulation trials. Figure 4.5 shows the average estimated percent spread using the RoN method compared to the LM percent spread for this scenario and shows a near one-to-one relationship

Figure 4.2: $\bar{\%}\sigma_{\hat{\tau}}$ as a function of $\bar{\%}\sigma_{\tilde{\tau}}$ in sufficiently sampled conditions.
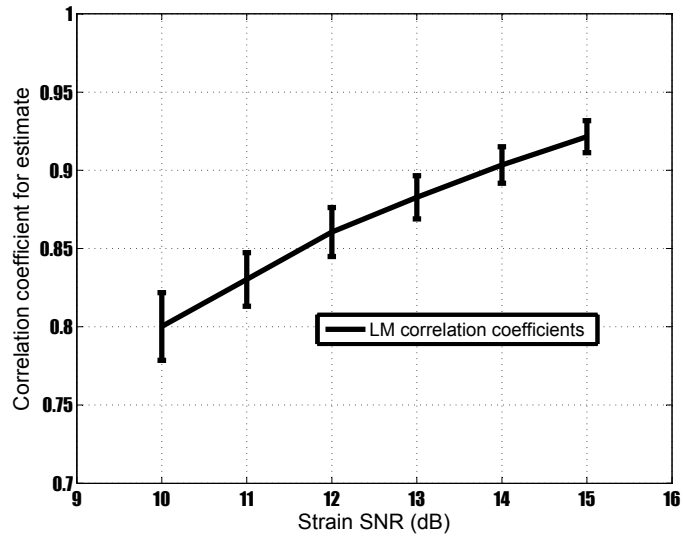
Figure 4.3: Average correlation coeefficient for LM estimates in sufficiently sampled conditions.
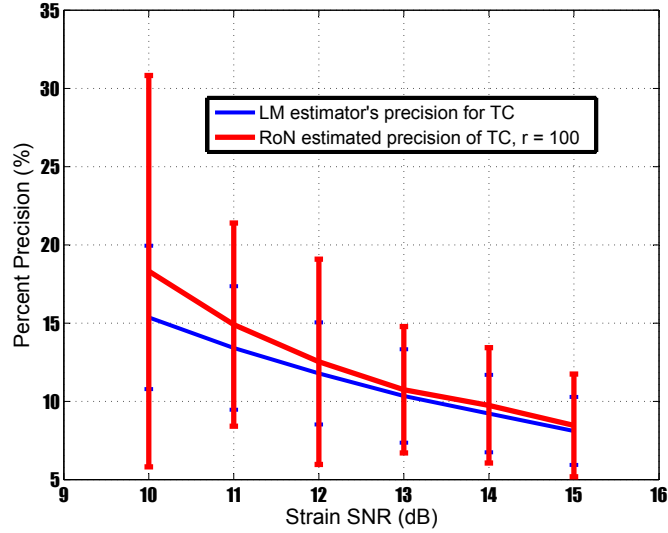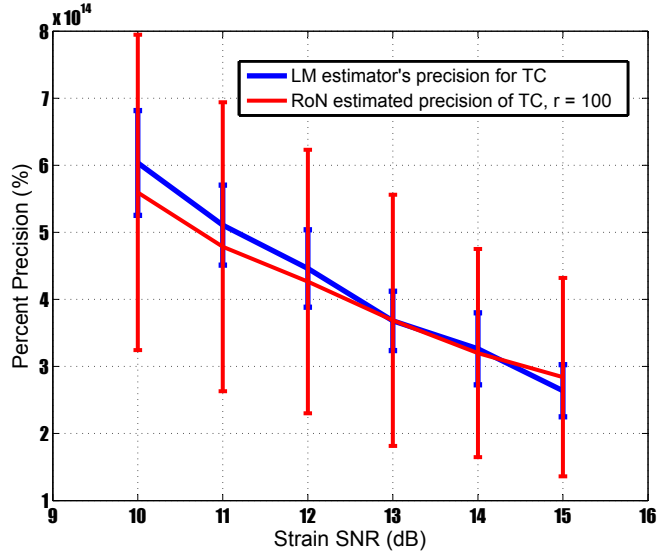
Figure 4.4: $\bar{\%}\sigma_{\hat{\tau}}$ and $\bar{\%}\sigma_{\tilde{\tau}}$ in insufficiently sampled conditions with RoN iterations $r = 100$.

between the RoN estimated precision and the precision of the LM algorithm. These figures show that the percent spread for the insufficiently sampled conditions is in the order of 10^{14}. The mismatch in results between Figures 4.1 and 4.4 and Figures 4.2 and 4.5 is consistent with the results in [50], which shows that under insufficiently sampled conditions, the TC estimate is subject to high error. Figure 4.6 shows the average correlation coefficient of the estimated TC curves using LM and the original noisy curve. As it can be seen, Figure 4.6 shows a near identical pattern to the results shown on Figure 4.3 despite the fact that prior studies have shown that estimate quality should be poor [50]. This indicates that CorrCoeff may not be a useful measure of estimate reliability.
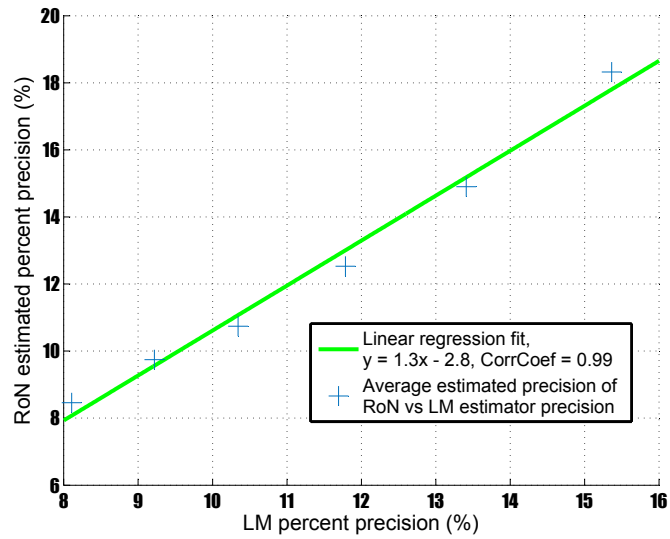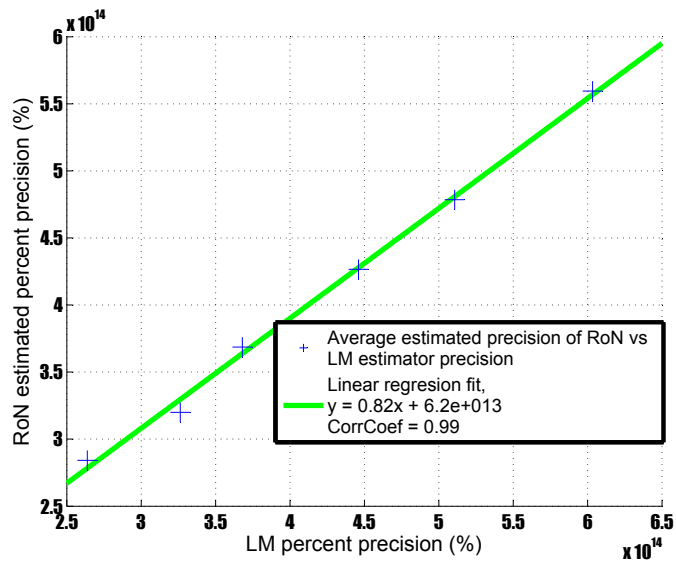
Figure 4.5: $\bar{\%}\sigma_{\hat{\tau}}$ as a function of $\bar{\%}\sigma_{\tilde{\tau}}$ in insufficiently sampled conditions.
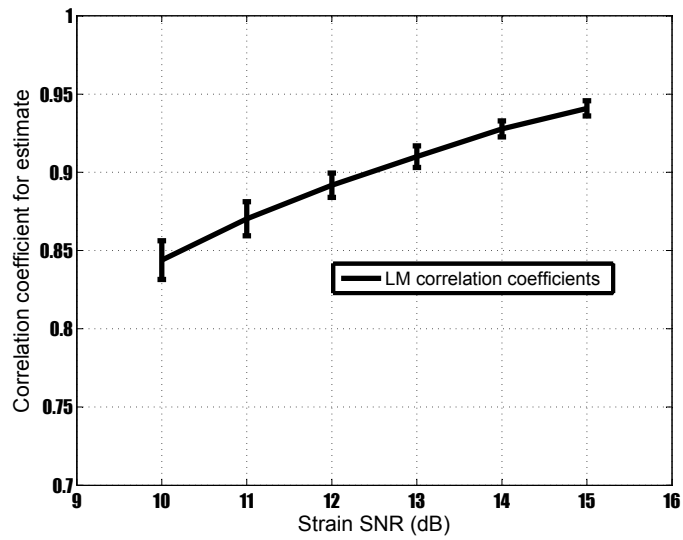
Figure 4.6: Average correlation coeefficient for LM estimates in insufficiently sampled conditions.

53
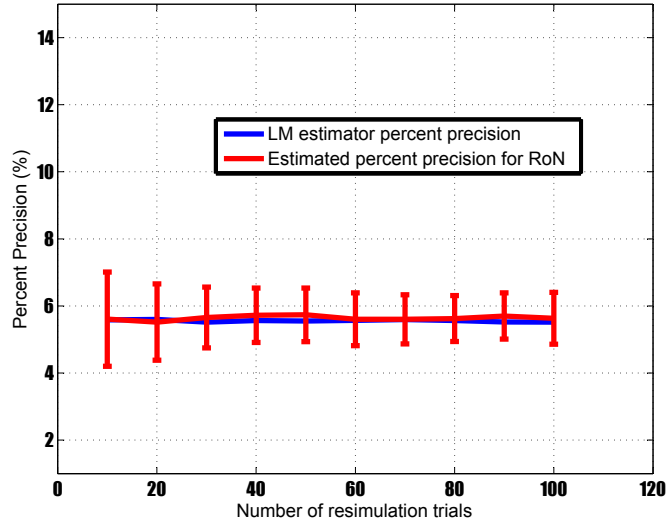
Figure 4.7: Progression of RoN precision estimator performance with respect to the number of resimulation trials r when strain $SNR = 15$, $\tau = 300$ and $\eta = 0.1$

4.4.1.3 Effects of number of resimulation trials on RoN performance

Figure 4.7 shows the results of of the RoN method performance dependence on r. As it can be seen, the average estimated percent spread is not statistically different as r changes. However the standard deviation of the percent spread estimates shows a decreasing tendency with respect to r in this case. The standard deviation of $\sigma_{\tilde{\tau}}$ is 1.4% in the case of $r = 10$ and decreases to 0.77% in the case of $r = 100$. This result shows that r has little bearing on the accuracy of $\sigma_{\tilde{\tau}}$, however more precise $\sigma_{\tilde{\tau}}$ estimates can be achieved with higher r, at the cost of increased processing time.

4.4.2 Experimental results

Figure 4.8 shows the τ image estimated using the LM method for WoO = 584 s, 484 s, 384 s, 284 s, 182 s, and 84 s. These figures show that the LM estimator, on

average produces a lower estimate for τ as the WoO decreases, which is consistent in the findings in [50]. Since most of the pixels of Figure 4.8(a) show TCs less than 150 s, this also means that all the WoOs considered are appropriate for TC estimation [50]. Figure 4.9 shows the SNR of the resulting τ images as WoO varies. The SNR does not monotonically increase or decrease as WoO increases. However, the figure shows that the difference between the maximum and minimum observed SNR is less than 1.5 dB. Figure 4.10 shows the average and standard deviation of the correlation coefficient of the estimates in these images. The average correlation coefficient shows a paradoxical decrease, but it does not decrease in a significant manner as the dynamic range of the averages shown in Figure 4.10 is less than 0.01 and also because the standard deviations (shown as errorbars) show overlaps in data between most point pairs of the graph. Also, the difference between the maximum and minimum average correlation coefficient is less than 0.015. Figure 4.11 shows estimated percent spread of τ estimates using the RoN method when $r = 100$. This figure shows that the percent spread of τ decreases as WoO increases in a significant manner (as the errobars do not overlap) until WoO $= 284$ s and shows that τ estimate reliability increases with respect to WoO. This result is consistent with previously published work [50] and is expected based on the nature of TC imaging, as the larger the WoO the signal has more time to manifest its properties.

4.5   Discussion

This chapter proposed, implemented, and analyzed a simple resimulation of noise time constant precision estimator for τ LSE estimates. Using 1-d simulations it showed that, using only one series of strain vs. time samples, the RoN algorithm can correctly track the spread of τ estimates. This estimated spread approximates the spread that the LM LSE estimator would display if it had several independent
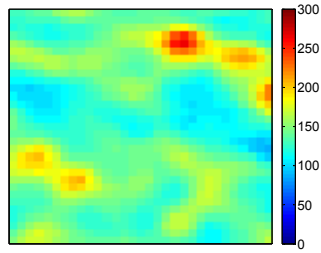
(a) WoO = 584 s
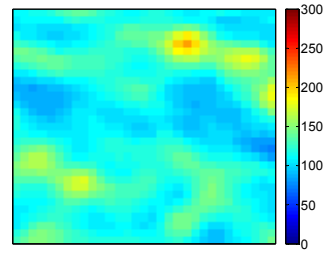
(b) WoO = 484 s
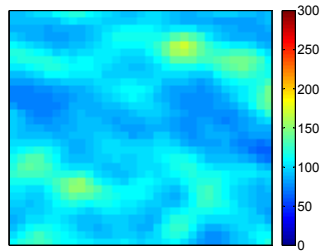
(c) WoO = 384 s
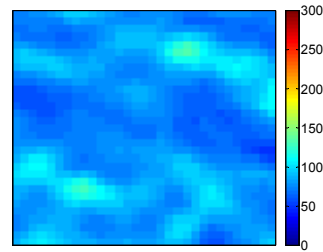
(d) WoO = 284 s
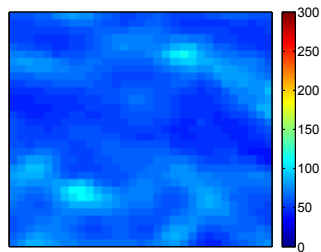
(e) WoO = 182 s
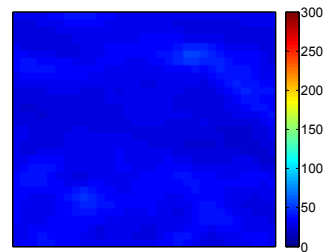
(f) WoO = 84 s

Figure 4.8: Estimated τ image in the region of interest at Different WoO.
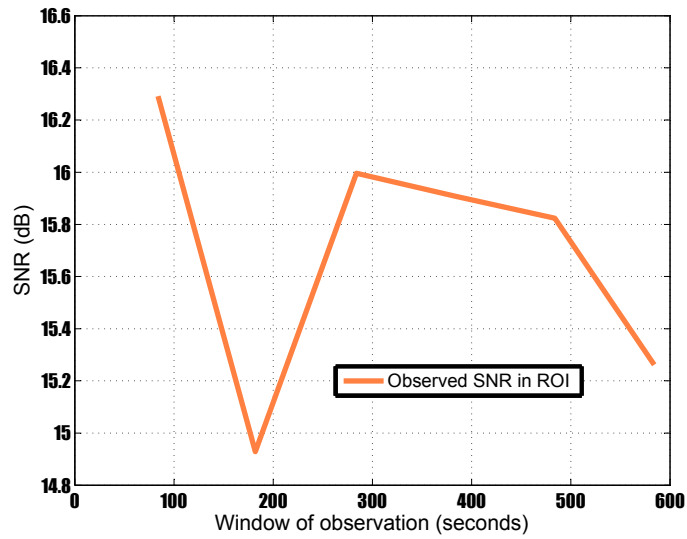
Figure 4.9: SNR of observed τ estimates vs WoO in the region of interest.
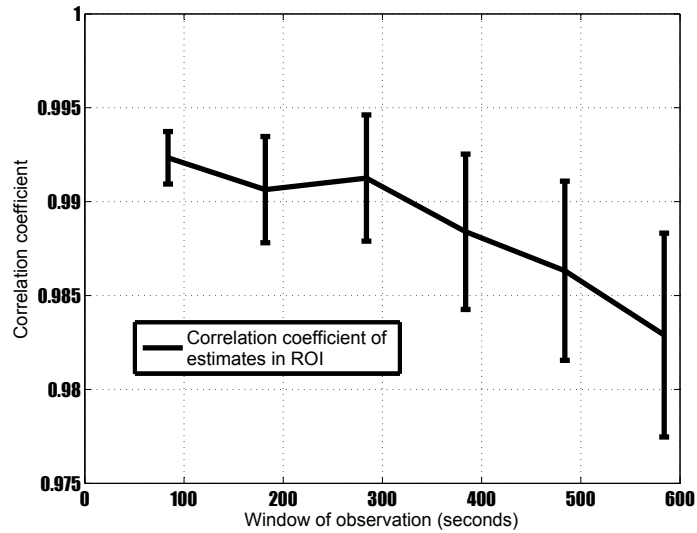
Figure 4.10: Average correlation coefficient for TC estimates vs WoO in the region of interest.
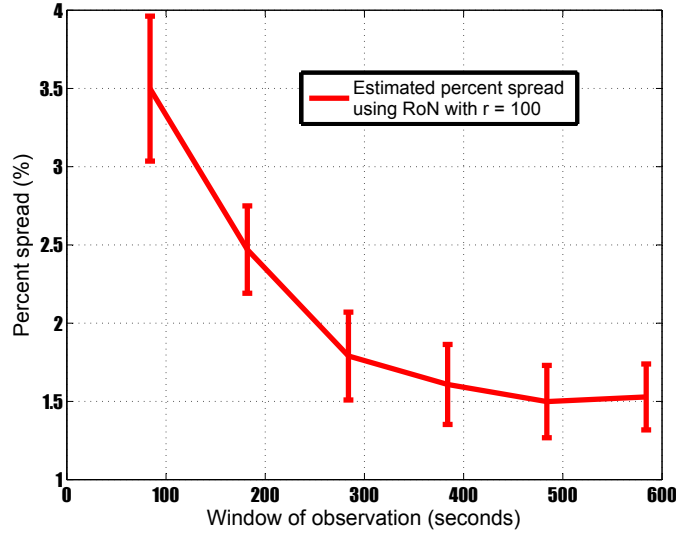
Figure 4.11: Average estimated percent spread vs WoO in the region of interest.

series of strain vs. time samples at a given SNR, τ, and η as shown in Figures 4.1, 4.4. However, as shown in both these figures, the spread of the precision estimates calculated using the RoN method is higher than the observable spread of the LM method. This increase in the spread of spreads should be expected, as the RoN method simply creates new samples to be fitted using the LM method itself. Figures 4.2 and 4.5 show that on average $\sigma_{\tilde{\tau}}$ and $\sigma_{\hat{\tau}}$ have a very strong linear relationship with a near 1 slope and near 1 correlation coefficient. In clinical scenarios, multiple experiments cannot be performed. Thus, the availability of the proposed method may provide a quick and reliable measure of the quality of the TC estimates.

Figures 4.3 and 4.6 show that the standardly used correlation coefficient estimate reliability is inadequate as both the sufficiently and insufficiently sampled cases show the same CorrCoeff values. This happens despite the fact that the LM estimator's

percent precision is on average less than 20% in the sufficiently sampled case and is in the order of 10^{14} in the insufficiently sampled case for all strain SNRs tested. Based on this investigation, the correlation coefficient provides an incorrect sense of estimator reliability. Similarly, a quality estimate based only on an image quality factor, such as the SNR, may also be misleading.

Figures 4.9 and 4.10 confirm the inappropriateness of using the correlation coefficient of estimates and visual appeal of resulting images as viable reliability measures. Previous findings [50] show that TC and EP estimate reliability should increase, the bigger the window of observation provided for data collection. However, these figures show that the correlation coefficient and observed SNR of TC images can give incorrect impressions about estimate reliability. Figure 4.11 shows that the RoN method can correctly track estimate reliability. This finding shows that the RoN method provides a more powerful measure of reliability than methods previously proposed for TC imaging.

Figure 4.7 shows that the RoN τ precision estimator, on average, accurately estimates the LM estimator's precision despite using only $r = 10$ resimulation trials. However, the decrease in the standard deviation of the the precision estimates shows that an increase in r will produce more precise precision estimates. This is an important observation which can cut down processing time when a quick, qualitative precision estimate is required.

The analysis of RoN shown in this work centers around its use for improving LSE estimation for poroelasticity and viscoelasticity imaging because it is a main topic of interest for this dissertation. However, it should be restated that the RoN method is meant to improve non-linear LSE estimation in general, and its use has the potential to impact fields outside of poroelasticity and viscoelasticity imaging or even ultrasound imaging itself. A full, in-depth analysis of the RoN method for general

use is outside the scope of this article but hopefully, the community will adapt the general structure of the RoN method for their specific use and further investigate its correctness.

Runtime considerations for the RoN algorithm were not analyzed in this paper because the runtime is mostly dependent on the number of RoN trials, r and the runtime of the LM LSE algorithm itself. Essentially, the RoN algorithm calls the LM LSE algorithm r times. The LM LSE algorithm, itself has been parallelized and implemented using a Graphics Processing Unit (GPU) successfully in [51] and is a real time algorithm. Since the RoN algorithm can be described as a series of independent processes, it is highly parallelizeable. The implementation and further refinement of the RoN algorithm for use with GPUs is left for future work. Its current runtime does not jeopardize its useability as a clinical tool.

It should be noted that complete experimental validation of the RoN method for poroelastic axial strain time constant imaging is currently a very challenging problem and should be tackled in future work. While, in this work, the preliminary experimental study shows that the RoN method does track the decrease in estimate reliability due to decreased sampling, experimentally examining if the RoN generated TC precision estimates closely follows the actual precision of TC estimates is not currently possible. The main reason for this is that there are currently no existing controlled poroelastic ultrasound phantoms with which repeatable experiments are possible.

4.6   Conclusion

This chapter implemented and analyzed the RoN precision estimator or least square error estimation. The precision estimator was tested for ultrasound axial strain time constant estimation. This testing showed that the RoN precision estima-

tor accurately estimates LSE estimator precision.

Indeed, the RoN estimator tracks how robustly the estimated curve fits the data. How well an equation fits a given set of data samples can be defined by how drastically the estimate changes with other data samples of similar level of mismatch. The devising of this reliability measurement in place, and the sampling requirements for TC estimation known, it is now possible to consider how well the single exponential time constant curve fits the axial strain data of non-homogeneous cases. With this preparation work done and understood, the next chapter of this dissertation discusses that problem.

5. SINGLE EXPONENTIAL TIME CONSTANT MODEL HAS THE POTENTIAL TO BE USED FOR NON-HOMOGENEOUS POROELASTICITY IMAGING

This chapter shows the culmination of the several years of preparation dedicated towards the simplification of mathematical modeling for poroelasticity imaging. Nearly 2 years of work were spent fine-tuning simulations to show that under certain conditions single exponential time constant imaging can serve as a potential imaging tool to image the poroelastic properties of tissues. As of this writing, the work shown in this chapter is being prepared as a manuscript for submission to a peer reviewed journal (likely Ultrasound in Medicine and Biology).

5.1   Introduction

In the past two decades technologies have been developed that allow physicians to acquire images that provide information on the mechanical properties of tissues [72, 55, 84]. Initially, ultrasound elastography concentrated itself on using quasi-static techniques that image the local strains in a tissue put under a compressive force ([54, 80, 83]). These methods generate images which, coupled with B-mode images, can help a physician's ability to diagnose underlying diseases and pathologies ([77, 80, 89, 25]).

Hidden in our understanding of mechanical properties is the fact that mechanical properties are merely parameters in the mathematical model which is chosen to model the physical behavior of tissues. In current clinical applications, the mechanical property of highest interest is the tissue's stiffness when the tissue is assumed to follow a Hookean behavior. In a Hookean tissue, the strain response to mechanical compression is completely linear with respect to the applied force and agnostic to

time ([72, 55, 84]). While the Hookean model has shown itself to be useful, over the past decade, literature has risen that suggests that further development of non-Hookean elastography will produce new and powerful diagnostic imaging modalities ([28, 36, 45, 57, 68, 73, 74, 87, 67, 65, 61, 38, 16]).

Among the non-Hookean elastography modalities, poroelastography refers to the application of elastography techniques for imaging the temporal behavior of materials that can be modeled as poroelastic media, due to their relative high fluid content and mobility ([38, 63, 64, 4, 5, 56, 2]). A poroelastic media is typically modeled as consisting of a solid matrix filled with a fluid ([61, 68]). While the origins of the study of porous media are in the study of soil mechanics ([79]), the interest in its investigation for the purposes of modeling tissues is clear as all tissues in multicellular animals are bathed in interstitial fluid and its flow is critical to tissue survival. For example, an understanding of underlying tissue poroelastic properties has already shown the potential for improvements in the diagnosis of certain cancers and lymphedema staging and tracking([47, 61, 6].

However, despite its potential for deep understanding of tissues, the mathematical complexity of the poroelastic models are perhaps the single-most impediment towards its clinical use in medical imaging. Even in the simplest case, of a homogeneous cylindrical material under creep compression, the time dependent mechanical response of the tissue is defined by an infinite sum of saturating exponentials ([2, 4]. To further complicate matters, all medical imaging is intrinsically premised on the fact that the region to be imaged is non-homogeneous. To the best of the authors' knowledge, no closed form expression exists that describes the time-dependent behavior of poroelastic materials with tumors to compressive forces.

Frequently, when the development of a closed form solution to a differential equation is difficult to find, the finite element method (FEM) is employed to find a nu-

merical solution to the problem ([60]). Advances in FEM have allowed its use in the study of poroelasticity imaging ([14]). In the past few years, there have been advances in parameter estimation that have developed a Least Square Error (LSE) based parameter estimator for single exponential time constant curves ([51]) and characterized its sampling requirements ([50]). Additionally, a method with which a sensible measurement of how well the single exponential time constant function fits the strain vs time relationship of a tissue have been developed ([49]. The purpose of this work is to combine these numerical techniques to explore how well a simple mathematical relationship involving a single saturating exponential function can fit the strain vs time behavior of non-homogeneous poroelastic properties.

5.2   Methods

5.2.1   Proposed equation

The single exponential time constant (TC) equation proposed to describe the local strain vs time behavior in a non-homogeneous poroelastic tissue is shown in equation 5.1.

$$s(t) = \eta + (\alpha - \eta)e^{-\frac{t}{\tau}} \tag{5.1}$$

where η is known as the equilibrium point (EP), α is the strain at time $t = 0^+$ and τ is the time constant (TC). LSE parameter estimation as well as methods to measure estimate reliability have been studied deeply and shown in previous literature [51, 50, 49]. It is worth nothing that equations similar to this have been used to describe the strain vs time behavior of viscoelastic materials under creep compression ([57]). Figure 5.1 shows plots of example strain vs time curves following equation 1.3 with the same equilibrium point and initial value but different time constants. Equation 5.1 is an assumed simplification based on the findings in [2] which derived that the

64
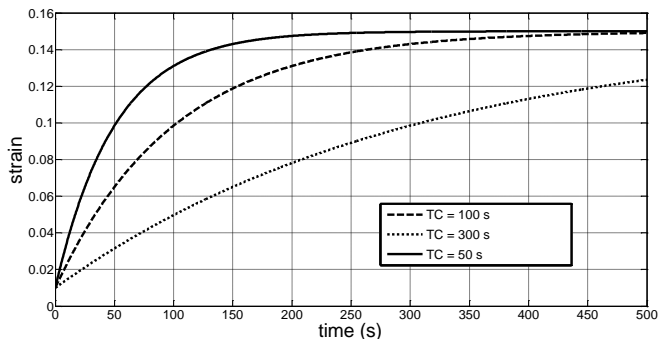
Figure 5.1: Example single exponential TC curves where the initial value is 0.01 and the equilibrium value is 0.15

strain response with respect to time of a homogeneous cylindrical poroelastic material under creep compression is described by an infinite sum of saturating exponentials.

5.2.2 Evaluation of equation suitability

In order to evaluate how suitably the single exponenential equation shown in Equation 5.1 describes the strain vs. time behaviour of a non-homogeneous poroelastic phantom an FEM study was realized.

A non-homogeneous poroelastic phantom placed under creep compression was simulated. The phantom's axial strain response was observed from time $t = 0$ until time $t = 500s$ in steps of $0.5s$. This sampling sequence was chosen following the findings in [50] in order to assure that inadequacies in sampling do not interfere with the quality of the LSE parameters estimation.

From the series of strain images, TC and EP images were generated by applying a Levenberg-Marquardt optimized TC estimator on a pixel-by-pixel basis. The TC estimator was developed in-house and the image generation process is described in depth in [51]. In order to measure how well the single exponential TC curve fit

the time-series of strain samples of each pixel, the reliability of the time-constant estimates was measured using the resimulation of noise (RoN) method as described in [49].

Finally, prior in-house research had hinted at the possibility that applying localized mean mask filters on each of the 1000 strain images required to create a TC image might improve the suitability of the single exponential TC equation. In order to study the effects mean-filtering would have on the measured reliability of mean mask-filters of different sizes were applied to the strain images and their effects on the measured reliability was studied. 2x2, 3x3, 4x4, 5x5, 6x6, and 7x7 square mean mask-filters were studied.

5.2.3 Resimulation of noise reliability measurement study

The findings in [49] showed that the resimulation of noise method was a method that could show the precision with which equation 1.3 fit a series of strain samples for a particular time constant and equilibrium point estimate. In this study, the percent estimated spread of time constant and equilibrium point estimates as their percent is referred to as their reliability and is shown in the following equations:

$$percent\,reliability\,\eta = 100 \times \frac{\sigma_{\tilde{\eta}}}{\hat{\eta}} \qquad (5.2)$$

$$percent\,reliability\,\tau = 100 \times \frac{\sigma_{\tilde{\tau}}}{\hat{\tau}} \qquad (5.3)$$

where $\sigma_{\tilde{\eta}}$ and $\sigma_{\tilde{\tau}}$ denote the estimated precision for the equilibrium point and time constant found by the RoN time constant precision estimator and $\hat{\tau}$ and $\hat{\eta}$ denote the time constant and equliubrium point estimates found by the LSE estimator. It is important to observe that *lower percent reliability measurement actually denote a more favorable fit.*
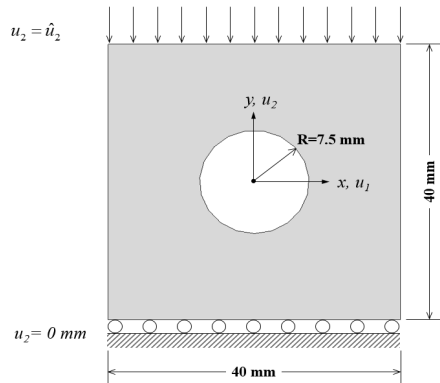
Figure 5.2: Description of cross-sectional area of simulated phantom

As has been shown in [49], this measurement of reliability has a tendency to flag bad fits by returning very large outlier values for the percent reliability. In order to see how reliable equation 1.3 fits the strain data of each pixel in a time constant image, the number of pixels in a time constant image that are considered acceptable is counted. An estimate is considered "acceptable" if its percent reliability is below a threshold.

5.2.4 Simulated phantom

For medical imaging, two non-homogeneous geometries of importance are the bi-layer scenario, which is relevant for lymphedema tracking, and the inclusion scenario, which is relevant to tumor imaging and potential cancer screening. This chapter focuses entirely on the inclusion scenario. To simulate a tissue with a tumor, a Finite Element Model phantom was simulated in the exact manner as described by [14]. The tissue is simulated as a rectangular prism with a cylindrical inclusion, both of infinite length. Figure 5.2 shows a description of the cross-section of this simulated phantom.

The software used to execute the FEM simulations was made in-house using
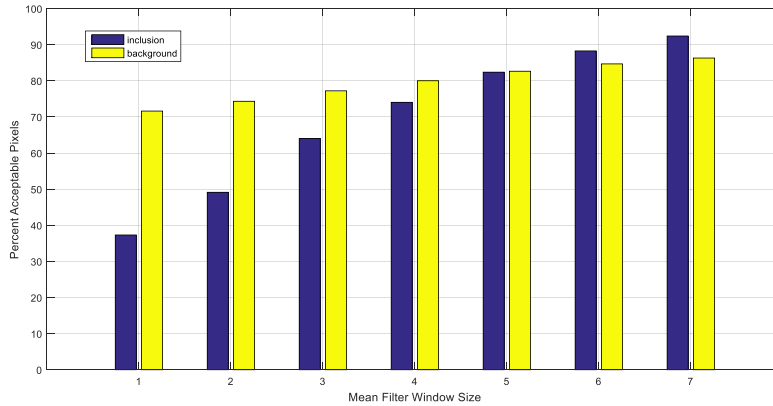
Figure 5.3: Average percent acceptable number of Time Constant estimates when the threshold is set to 5 percent

methods described by [60]. The only parameters that were controlled for the study were the Poisson's Ratio of the solid matrix (μ_s), the Young's Modulus of the solid matrix (E_s) and the permeability. For all simulated phantoms, both the inclusion's and the background's Poisson's Ratio was set to 0.25. A total of 25 parameter contrast cases were studied. Contrast combinations in both k and μ_s were studied.

5.3   Results

5.3.1   Effects of spatial averaging on estimated reliability

Figures 5.3, 5.4, 5.5 show a study of how the size of the mean filter applied to the strains affects the average number of acceptable pixels in the inclusion and the background when the threshold of acceptability is set to 5%, 10%, and 15% respectively. These figures show that the reliability of TC estimation is consistently non-decreasing as the mean filter window-size increases. In figure 5.3, when the definition of acceptability is strictest, the effects of filtering appear most dramatic. The figure shows that when no filter is applied, less than 40% of all pixels in the inclusion are considered acceptable, but when a 7x7 mean filter is applied, more than 90% of pixels in the inclusion are acceptable.

Figure 5.4: Average percent acceptable number of Time Constant estimates when the threshold is set to 10 percent

Figure 5.5: Average percent acceptable number of Time Constant estimates when the threshold is set to 15 percent
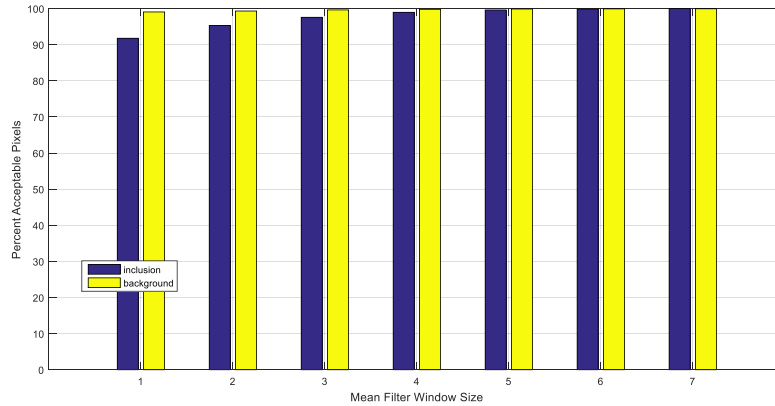
Figure 5.6: Average percent acceptable number of Equilibrium Point estimates when the threshold is set to 1 percent

Figures 5.6, 5.7, 5.8 show a study of how the size of the mean filter applied to the strains affects the average number of acceptable pixels in the inclusion and the background when the threshold of acceptability is set to 1%, 3%, and 5% respectively. As is the case with Figures 5.3, 5.4, and 5.5, these figures show that applying a mean averaging filter on the strains improves the reliability of the equilibrium point fit. These figures show that the estimation of the equilibrium point is more robust than time constant estimation. As shown in figure 5.6, even in the strictest definition of acceptability, over 90% of all pixels in the inclusion and background are considered acceptable when no filter is applied on the strains. The superior robustness of the equilibrium point estimates is consistent with the findings in [51, 50].

5.3.2   Effect of E_s and k on time constant estimates

Figures 5.9, and 5.10 show the time constant images, time constant reliability and equilibrium point images of all studied cases when a 7x7 mean filter was applied to the strain images.

It is worth noting that in figure 5.9, the colorbar is the same for the top 3 rows, where the inclusion is more permeable than the background. The colorbar range
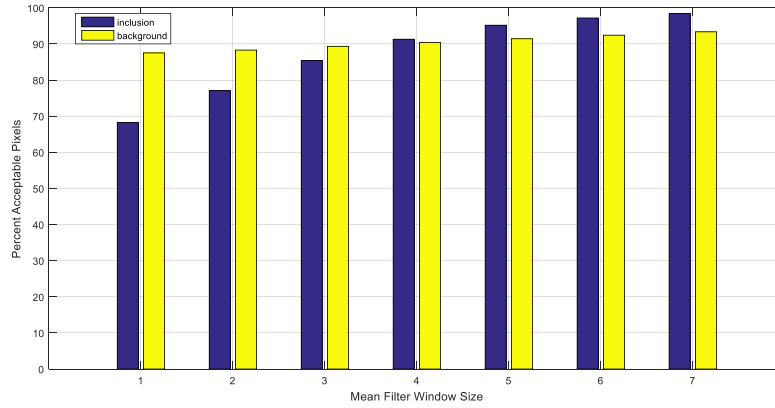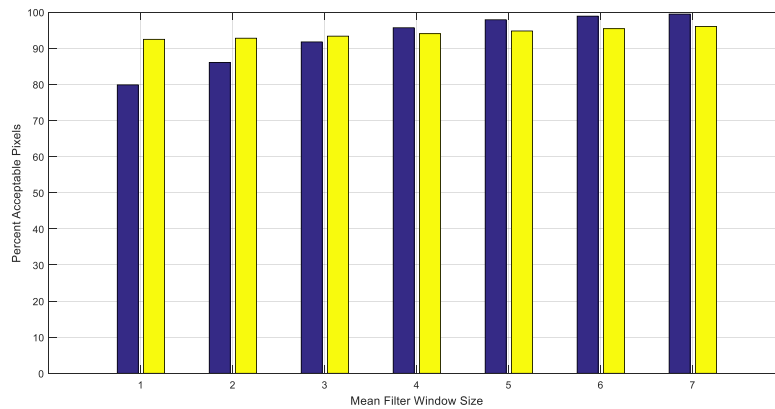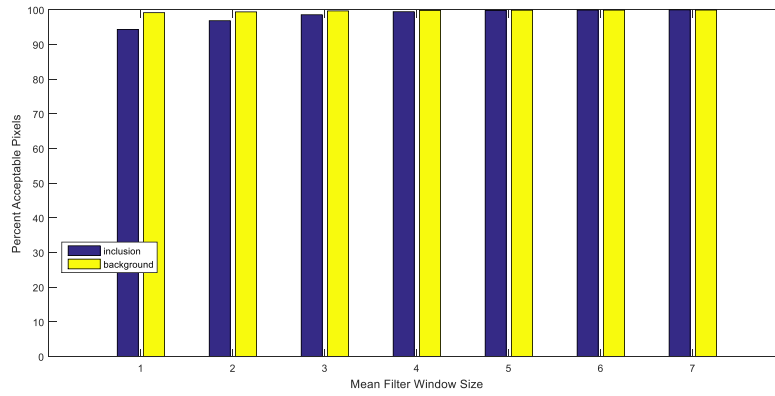
Figure 5.7: Average percent acceptable number of Equilibrium Point estimates when the threshold is set to 3 percent
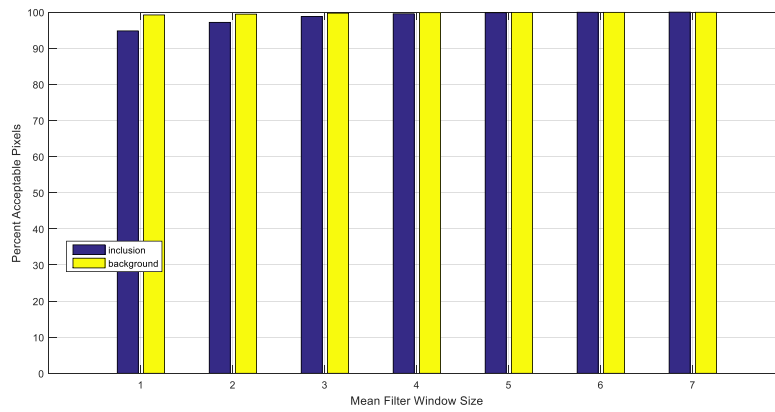
Figure 5.8: Average percent acceptable number of Equilibrium Point estimates when the threshold is set to 5 percent
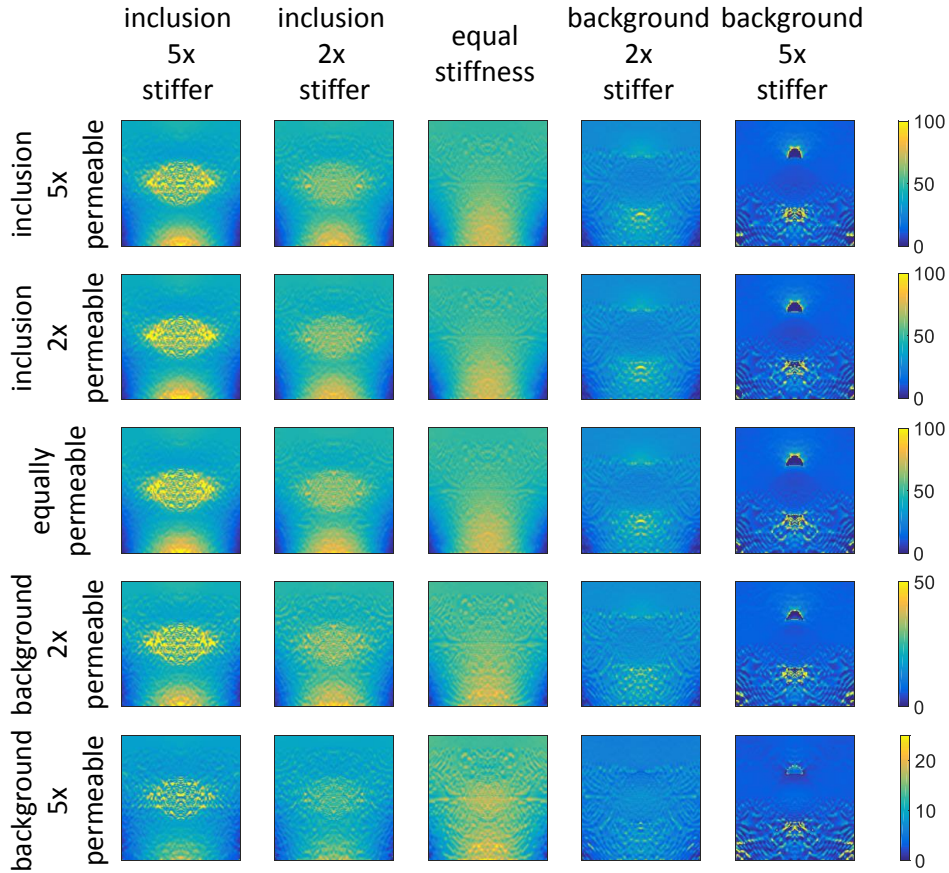
Figure 5.9: Time constant images of all studied cases

had to be reduced for the bottom 2 rows of this figure so as to allow the display of the inclusion. This shows that when the background is more permeable than the inclusion there is a visible and dramatic reduction in the time constants of the entire image. However, the images also show that an increased permeability in the inclusion does not manifest itself as a change in the time constant images. This would suggest that the background's permeability plays a dominant role in time constant imaging. This is consistent with the findings in [14].

Figure 5.10 shows that the underlying stiffness, E_s, and permeability k contrast have an effect of the reliability of time constant estimates. For all cases there are
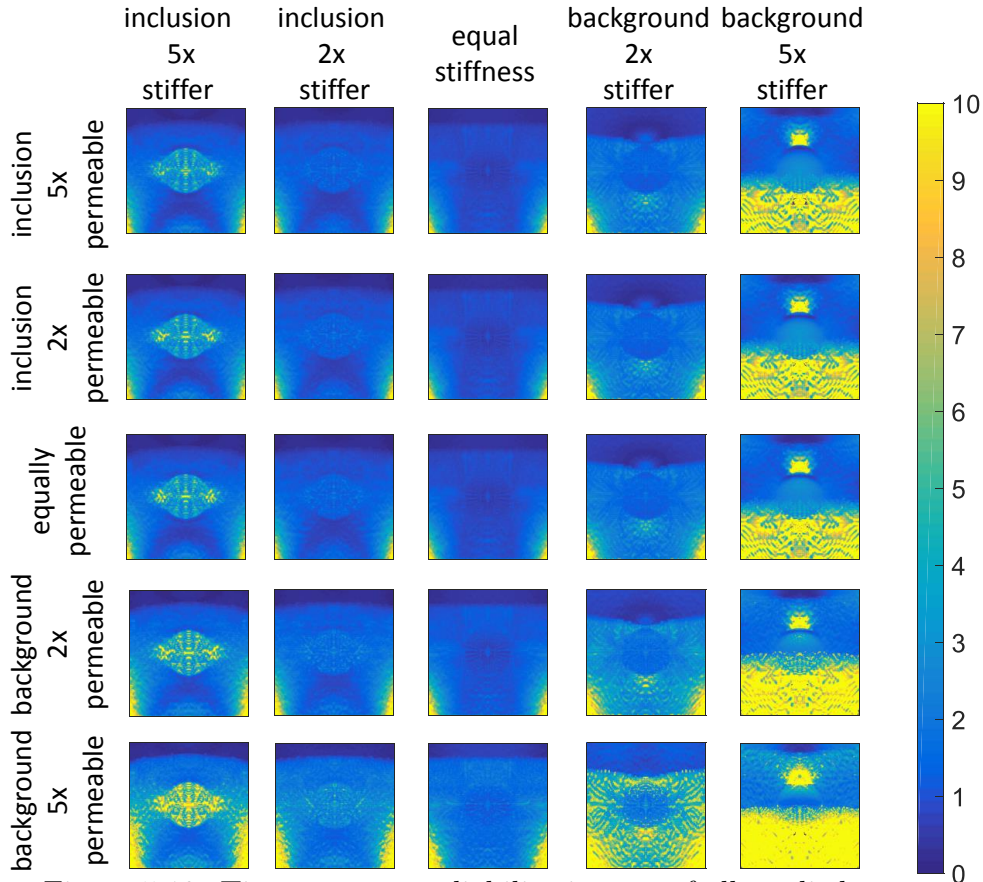
Figure 5.10: Time constant reliability images of all studied cases

regions in the bottom left and right corners where the time constant estimate reliability is above 10%. The figure also shows that, in the cases where the background is 5 times stiffer than the inclusions, nearly the entire bottom half of the images show time constant reliabilities above 10%, suggesting that the simplified single exponential model maybe unsuitable for this scenario.

Figures 5.11, 5.12, 5.13 show how the underlying E_s contrast affects the average number of pixels in time constant images that are considered acceptable. Of note in figure 5.13 is the fact that even when the threshold of reliability is loosest, less than 80% of all time constant estimates in the background are considered acceptable

Figure 5.11: Average percent acceptable time constant estimates with respect to stiffness contrast when the threshold is set to 5 percent.

when the background is 5 times stiffer than the inclusion.

Figures 5.14, 5.15, 5.16 show how the underlying k contrast affects the average number of pixels in time constant images that are considered acceptable. These figures show that there is a decrease in time constant estimate acceptability as the background becomes more permeable than the inclusion. As shown in figure 5.9 the time constant estimates show a decreasing tendency as the background permeability increases. The study of sampling requirements shown by [50] shows that for the same time sampling frequency of strains, the quality of time constant estimation worsens as the time constant becomes smaller. However, figure 5.16 shows that when the measure is loosened to 15%, in all contrast cases, more than 90% of all time constant estimates are acceptable. The figures show that the acceptability of the TC estimates is the same for the cases where the inclusion is more permeable than the background and the case where there is on contrast in permeability. This behavior is predictable

74

Figure 5.12: Average percent acceptable time constant estimates with respect to stiffness contrast when the threshold is set to 10 percent.

Figure 5.13: Average percent acceptable time constant estimates with respect to stiffness contrast when the threshold is set to 15 percent.

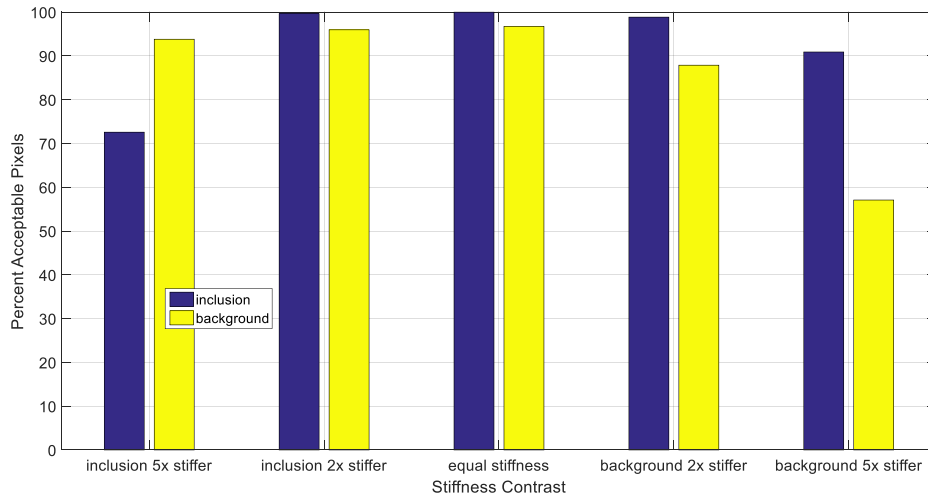Figure 5.14: Average percent acceptable time constant estimates with respect to permeability contrast when the threshold is set to 5 percent.

from figures 5.9 and 5.10, because an increase in inclusion permeability contrast has no observable effect on the time constant images.

5.3.3 Effect of E_s and k on equilibrium estimates

Figure 5.17 shows the equilibrium point images for all the different underlying contrast scenarios studied when a 7x7 mean averaging filter is used. The figure shows that the equilibrium point estimates are not dependent on the underlying permeability contrast but only on the underlying stiffness, E_s. This is consistent with findings in previous literature ([2]). Since 5.6 shows that for this filtering scenario, nearly 100% of all pixels are acceptable even when the threshold is set to 1%, an in-depth study of how E_s and k contrast affects equilibrium point estimate acceptability would be uninteresting and is not reported.
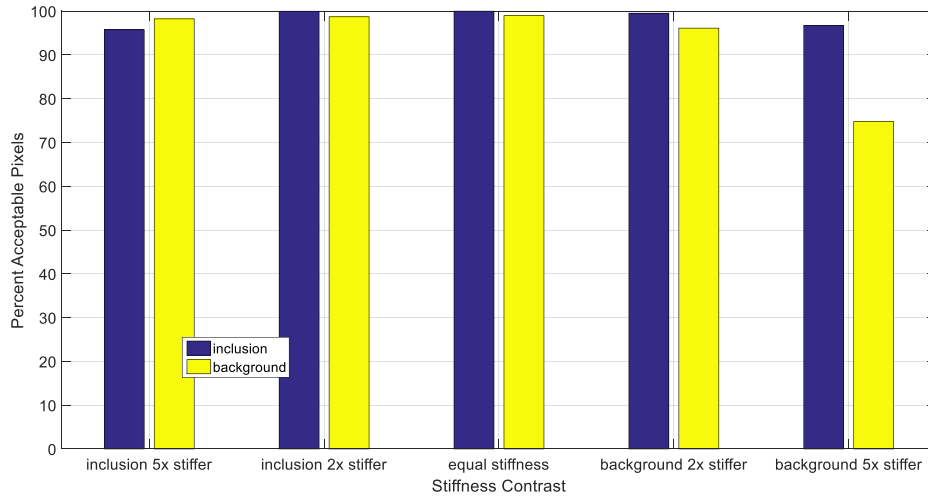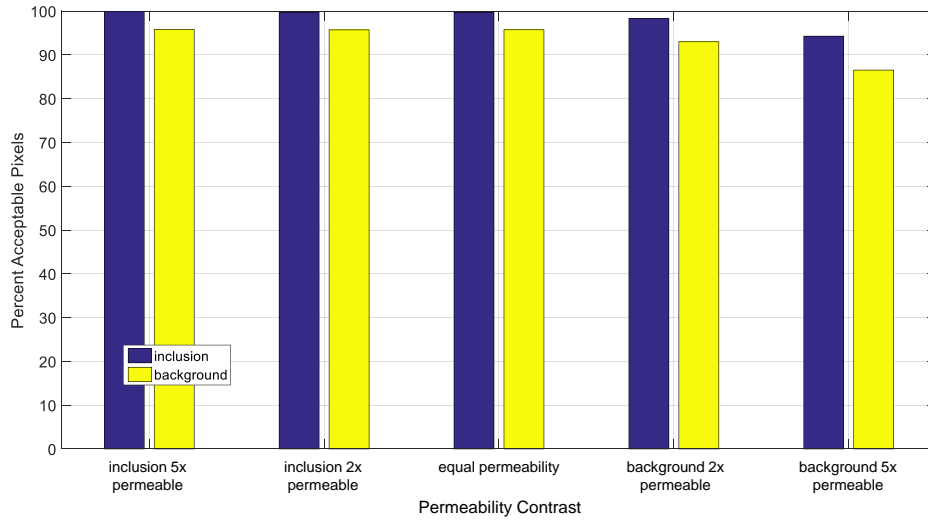
Figure 5.15: Average percent acceptable time constant estimates with respect to permeability contrast when the threshold is set to 10 percent.
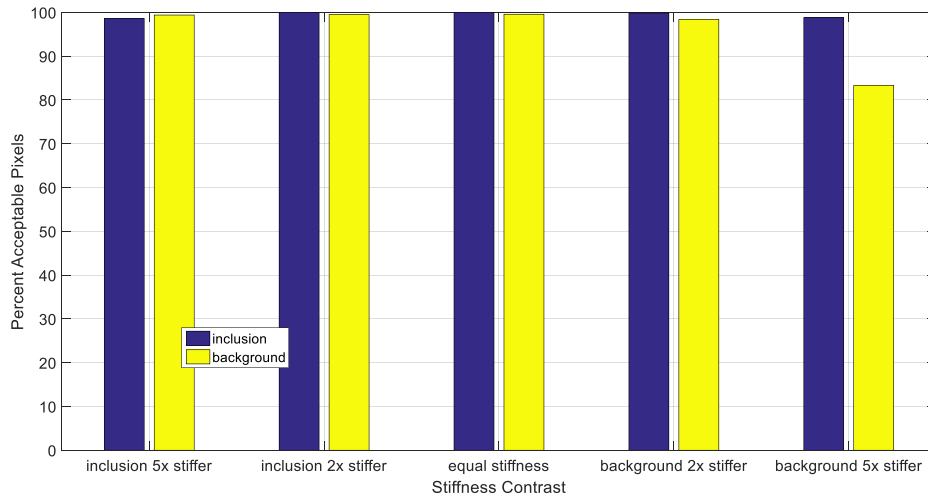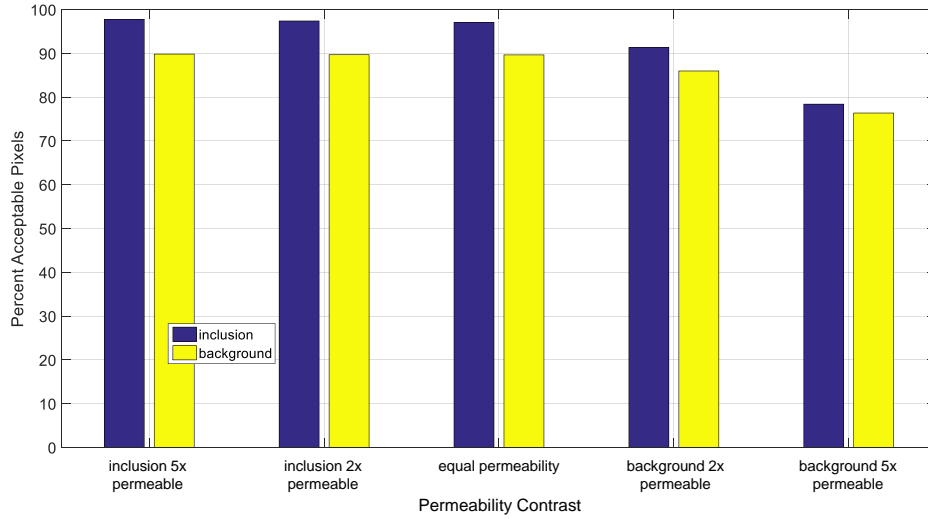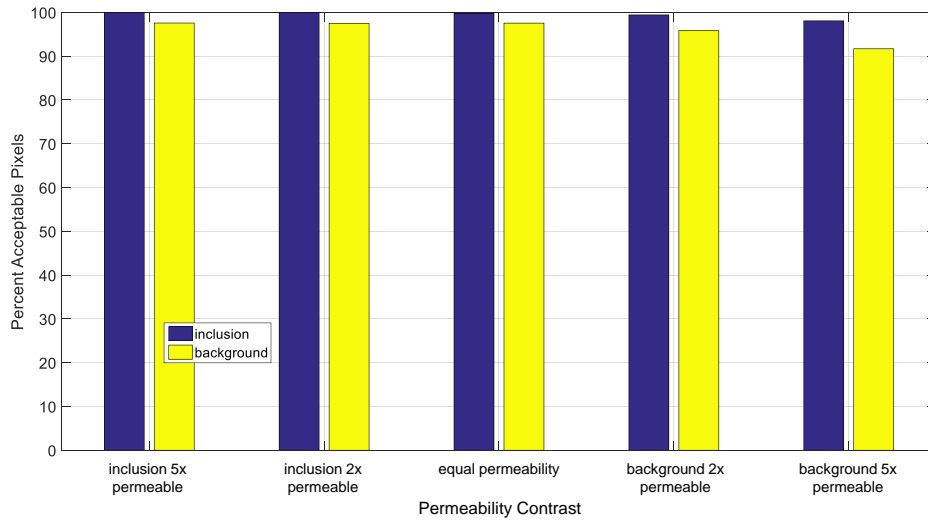

Figure 5.16: Average percent acceptable time constant estimates with respect to permeability contrast when the threshold is set to 15 percent.
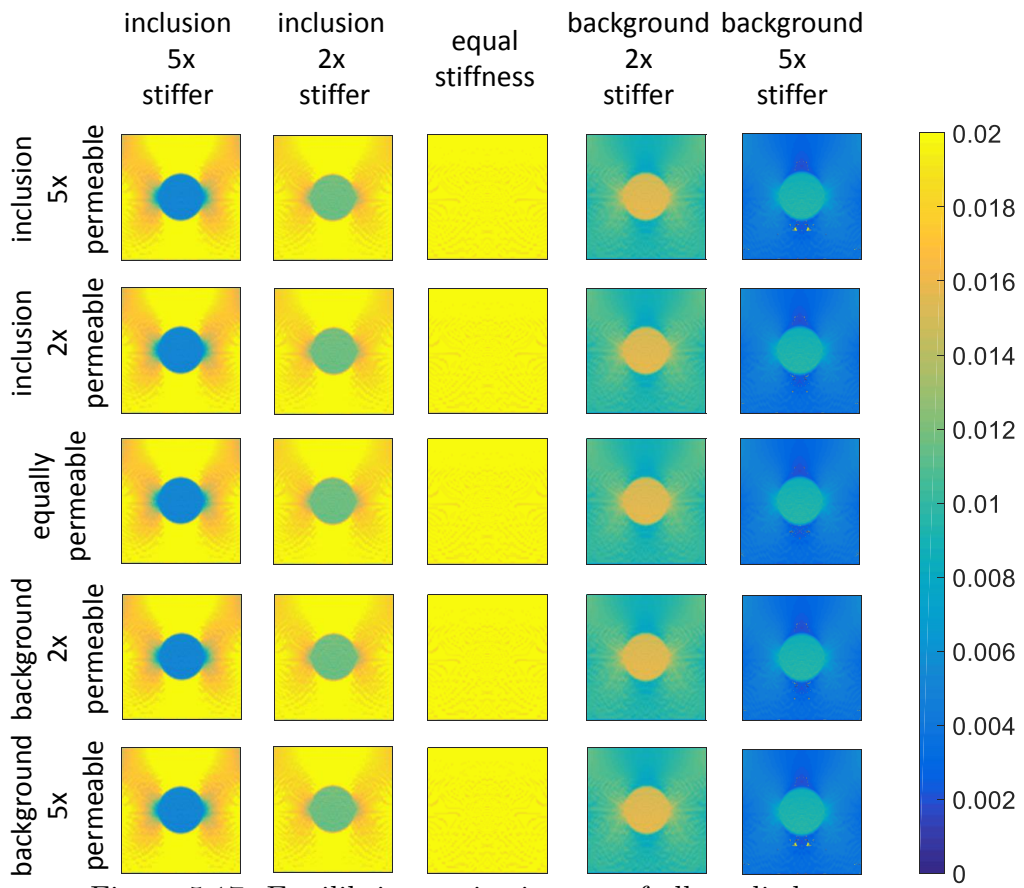
Figure 5.17: Equilibrium point images of all studied cases

5.4   Discussion

The end-purpose of a mathematical model or equation is to define the relationships of different observable physical phenomena. It is likely that the current complexity of the equations surrounding the observable mechanical behavior of poroelastic materials with ultrasound strain elastography have caused the field to stagnate. While a simplified relationship, as shown in 5.1 has frequently been suggested or hinted at by previous works [51, 50, 49, 63], the model has been frequently criticized for being unverified. This work has aimed to show that the simplified mathematical model has the potential to be useful for poroelasticity tumor imaging because the time-series of observable data indeed fits the single exponential time constant model.

Figures 5.9 and 5.10 suggest that the model may be unsuitable for the case in which the background is stiffer than the inclusion. However, this scenario is clinically uninteresting for poroelasticity imaging as inclusions that are softer than the background are often fluid filled cysts which can be easily diagnosed with standard ultrasound B-mode imaging. However, for all other cases studied, the equation suitably describes the strain behavior of more than 90% of a poroelastic tissue with an inclusion within at most a 15% spread when a 7x7 mean filter is applied to the localized strain measurements. As shown in figures 5.3, 5.4 and 5.5, increasing the size of the averaging filter improves the suitability of the fit, though it would certainly come at the cost of a decreased spatial resolution in the time constant and equilibrium point images.

This study has also shown the effects underlying permeability and stiffness contrasts have on the measured time constant and equilibrium point images. When the background is more permeable than the inclusion, a lowering in the time constant estimates of the entire image can be observed. In the cases where the inclusion is

more permeable than the background, the time constant images show no appreciable difference from the time constant images calculated when the background and the inclusion were equally permeable. These observations would suggest that the background's permeability plays a dominant role in the time constant estimates of the entire region of interest. When considering that the time dependent strain behavior of poroelastic tissues is highly characterized by the fluid flow behavior, it can be reasoned that the background appears to act as a limiter on the inclusion. The background's dominance can be explained by the fact that for fluid to exude out of the inclusion, it must flow into the background.

This study has shown that the time constant images are dependent on the permeability and also the stiffness. This study has also shown that the equilibrium point images seen are completely dependent on the stiffness contrast of the images. Indeed, an in-depth study of how permeability and stiffness affect both the time constant and equilibrium point images, so as to be able to measure the permeability and stiffness distribution of the region of interest from these images alone is well beyond the scope of this study. However, the fact that the equilibrium point images are only dependent on the stiffness contrast of the images suggest that they could be used to isolate the underlying stiffness distribution. This isolated stiffness distribution information could then be used to enhance the permeability information that we have demonstrated is present in the time constant images.

Finally, this study showed a "back-door" FEM-aided approach to simplification that has not been used before. Ideally, one would want to conduct experiments using tissue mimicking poroelastic phantoms instead of having to rely solely on FEM simulation phantoms. However, the challenge with this is that, as of this writing, there are no poroelastic phantoms with which one can conduct experiments to corroborate the findings in the FEM-aided approach. While tofu has been frequently used for

this [51, 50, 49, 63], experiments with controlled permeability and stiffness are not yet possible. Additionally, the mathematical complexities regarding poroelasticity imaging have been significant enough, that it would be difficult to interpret the results from such experiments, even if they could be executed. Indeed, what this work is attempting to accomplish is to simplify these mathematical complexities so that poroelasticity imaging experiments can be carried out and successfully interpreted.

5.5   Conclusion

This work and indeed this entire dissertation tested if a simplified saturating single-exponential equation can describe the strain-vs-time behavior of a non-homogeneous poroelastic tissue with an inclusion. The quality of fit was measured using the resimulation of noise method. The study showed that the simplified model has the potential to be useful for clinically relevant poroealasticity tumor imaging.

6. PROPOSED FUTURE WORK AND CONCLUSION

This chapter discusses recommendations on how to expand the findings of this dissertation so as to improve the field of medical ultrasonic poroelasticity imaging. The field is complex and even with the work completed in this dissertation is far from being an acceptable clinical tool. Indeed, the completion of the recommendations made here will not themselves make the jump towards clinical use, but it's likely that they will be a push in the correct direction.

6.1 Scientific improvements

6.1.1 Time constant images to parameter contrast

This dissertation confirmed that the single exponential saturating model theoretically fits the axial strain vs time response of a non-homogeneous poroelastic tissue under creep compression. However, the usefulness of this fit is still in question as the translation of time constant and equilibrium point maps to poisson's ratio, permeability and stiffness maps is non-trivial.

At the onset of this study, it was my belief that the time constant contrast would give information about permeability contrast. Figure 6.1 shows the time constant figures when the inclusion is stiffer than the background along with the ratios of the average time constant of the inclusions, τ_i, and the average time constant of the background, τ_b. These images show that time constant ratio is strictly increasing with respect to the stiffness contrast in the images as every image in that figure has a smaller ratio than the one to its left. However, there is no easily recognizable pattern between the time constant ratios and the permeability contrast. While the pattern is clear with respect to the stiffness, that information is reflected more efficiently in the equilibrium point images.
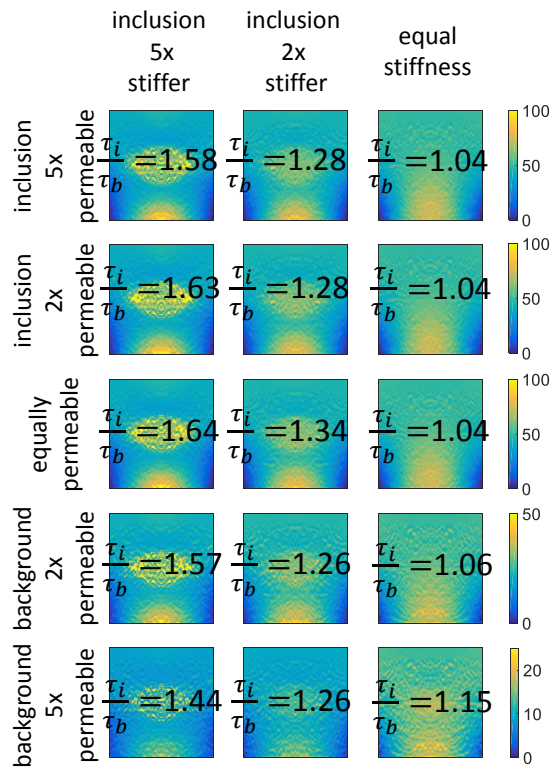
Figure 6.1: Time constant ratios when the inclusion is stiffer than the background

That fact does not, in itself, kill the field of poroelasticity time constant imaging. It is clear from figure 6.1 that when the background permeability contrast increases, the time constants in the entire image decrease. Furthermore, it is common in clinical studies to see background permeability contrasts of more than 5x. Figure 6.2 shows simulated time constant figures when the background is more permeable. Generally, after the background is more than 5 times more permeable than the inclusion, there is a more noticeable increase in time contrast contrast.

6.1.2 Considerations of multiple exponentials

At the onset of the study, it was conjectured it was very likely that a sum of multiple exponentials like in 6.1 would more suitably fit the axial strain vs time data from a creep experiment.

$$s(t_i) = \sum_{k=1}^{k=m} \eta_k + (\alpha_k - \eta_k)^{-\frac{t}{\tau_k}} \tag{6.1}$$

However, when attempts to implement the LSE estimator when $m = 2$ for this model, it became clear that it brought in more complications than clarifications. As mentioned earlier, the LSE estimator operates by minimizing the LSE. When attempting to find the parameters τ_k and η_k that minimize the Least Square Error, it becomes clear that the optimization problem is not convex. This is evident by the fact that the τ_k from the above equation are interchangeable. Furthermore, interpretation of how the set of τ_k and η_k are affected by poisson's ratio, permeability and stiffness becomes more complicated. As poroelasticity imaging is complicated enough and the single exponential equation has already been shown to be rich with possibilities, investigating this more complicated model is at this moment not required.
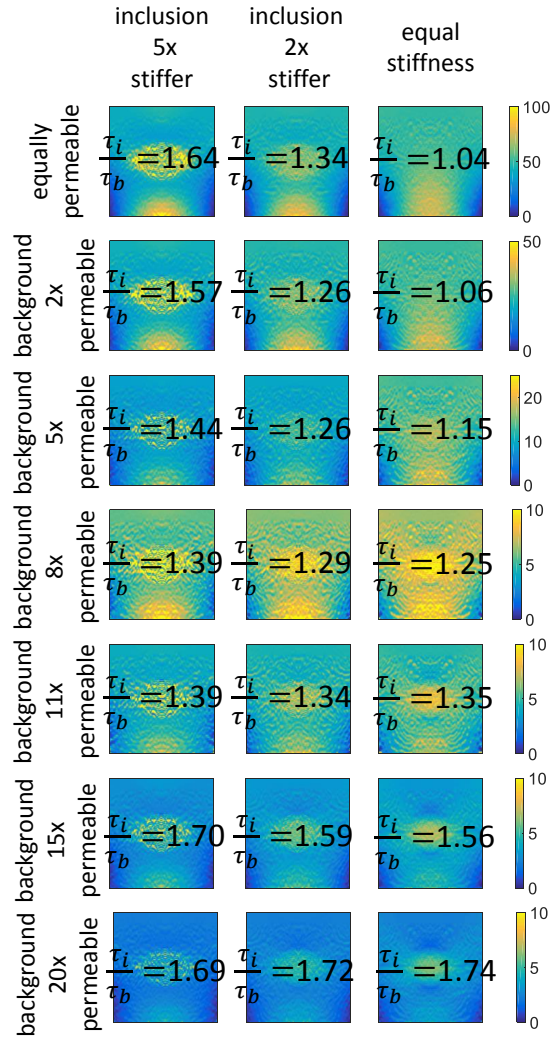
Figure 6.2: Time constant rations when the inclusion is stiffer than the background and the background is more permeable than the inclusion

6.2 Engineering improvements

6.2.1 FEM runtime improvements

The work shown in this dissertation required an extensive FEM study. To carry out the scientific improvements suggested in this chapter would require a significant extension of these simulations. However, the processing time requirements for doing this in a similar fashion to the way this study was realized would make this prohibitively time-taking.

Almost all FEM simulations for this study were run on a Windows machine equipped with a Core i5 4460 processor and 8 GB of 1600 MHz RAM. Even with this equipment, the FEM simulations would take on average 3 hours to complete successfully. This estimate does not include the number of FEM simulations that were deemed unsuccessful due to bad setup of time sampling requirements. While, indeed, this is a vast improvement over the runtimes the TAMU ultrasound lab experienced 3 years ago, it still makes efficient use of manpower difficult.

In the past decade the use of graphics cards for scientific computations has become prevalent [10, 33, 15]. They have even been used to accelerate FEM simulations [13, 34]. GPUs have shown the potential to speed up computationally intense procedures by orders of magnitued [10]. Implementation of Poroelasticity FEM simulations in GPUs could significantly accelerate ultrasound poroelasticity time constant imaging research.

6.2.2 Resimulation of noise improvements

GPU acceleration would not only improve the actual execution of FEM simulations. As has been shown in [49], the resimulation of noise method used to create fit reliability maps is extremely parallelizeable and therefore an excellent candidate for GPU acceleration. Indeed, the field of medical imaging frequently employs GPU

acceleration [21]. The TAMU ultrasound lab is no stranger to GPU implementations [88] and indeed the LM optimized LSE estimator has itself been accelerated with a GPU [51].

In the simulation procedure used in this dissertation, the employment of the resimulation of noise method to generate reliability maps is time taking. With the hardware used to create the FEM simulations, applying the resimulation of noise method takes around 4 hours per case. Implementing this algorithm to a GPU could reduce this to runtime to the order of minutes [51]. This would not only be an improvement to research. It would also allow for the quick generation of reliability maps in clinical scenarios.

6.2.3   Experimental improvements

A frequently recurring theme seen in poroelasticity imaging is the lack of controllable ultrasound poroelasticity phantoms [51, 50, 49, 14]. Extensive work in the field of poroelasticity imaging has been done using tofu, however, it is becoming clear that tofu phantoms are inconsistent because experiments cannot be conducted with control of stiffness, Poisson's ratio and permeability. Moreover, creating non-homogeneous poroelastic phantoms with a connected inclusion, as of this writing, have not been invented.

Anuj Chaudhry has made some recent advances in the TAMU ultrasound group with regards to poroelastic phantoms. Chaudhry has extended polyacrylamide-based gel phantoms, which were previously used in ultrasound viscoelasticity imaging [41], to become suitable for poroelasticity ultrasound imaging research. These new gel phantoms' pore size and stiffness can be controlled. As well, his initial findings show that it is possible to create poroelastic connected inclusion phantoms from them. However, the phantoms still need some more investigation to mature into a viable

tool for poroelasticity imaging research. They should certainly be studied and should be used to corroborate the findings in this dissertation.

Along with Chaudhry's polyacrylalamide-based gel phantoms, it would be interesting to consider the employment of 3-d printing to generate phantoms. Currently, sub-millimeter resolution 3-d printed phantoms have been characterized for the use for MRI and CT [8]. Recent literature has also employed 3-d printing to aid in the creation of medical ultrasound tissue mimicking phantoms [17]. While it is still farfetched to consider directly printing micrometer sized pores directly to create a phantom, it should be possible to use 3-d printers to control phantom geometries.

6.3 Conclusion

Even with the work developed for this discussion, ultrasound poroelasticity imaging is still far from being a clinically viable tool for diagnosis. However, it is important to note that tissues should theoretically be poroelastic because all living tissue has a high fluid content that is required to flow through it for survival. Progress in the field has been slow for various reasons. Perhaps the extreme mathematical complications that arise in the poroelastic model coupled with the fact that linear and viscoelasticity imaging are still extremely fruitful despite having less complications can explain why medical poroelasticity imaging's slow progress.

This dissertation proposed that the single exponential time constant equation could describe the strain vs time behavior of a non-homogeneous poroelastic material. The work shown in here extensively expanded knowledge about least square error estimation for time constant curves. Additionally a reliability measurement which correctly showed the precision with which a least square error estimated curve fit experimental data was developed as well as implemented and tested for single exponential time constant curves. This reliability measurement was then used to see

how well the curve fit simulated experiments. This work showed that under scenarios of clinical interest, the single exponential time constant curve, fit, within 10% precision the strain data for over 90% of all data in the non-homogeneous simulated phantom when a mean average mask filter was applied on the localized strain data.

REFERENCES

[1] J J Ammann, R Rivera, and J Ophir. Rheological modeling of the time-dependent behavior of poroelastic materials under creep test experiments. In *5th International Conference on the Ultrasonic Measurement of Tissue Elasticity*, Snowbird, Utah, USA, 2006.

[2] C G Armstrong, W M Lai, and V C Mow. An analysis of the unconfined compression of articular cartilage. *J Biomech Eng.*, 106:165–173, 1984.

[3] J S Bendat and A G Piersol. *Random Data. Analysis and Measurement Procedures.* John Wiley and Sons, New York, 1986.

[4] G P Berry, J C Bamber, C G Armstrong, N R Miller, and P E Barbone. Towards an acoustic model-based poroelastic imaging method: I. theoretical foundation. *Ultras. Med. Biol.*, 32(4):547–567, 2006.

[5] G P Berry, J C Bamber, N R Miller, P Em Barbone, N L Bush, and C G Armstrong. Towards an acoustic model-based poroelastic imaging method: Ii. experimental investigation. *Ultras. Med. Biol.*, 32(12):1869–1885, 2006.

[6] G P Berry, J C Bamber, P S Mortimer, N L Bush, N R Miller, and P E Barbone. The spatio-temporal strain response of oedematous and nonoedematous tissue to sustained compression in vivo. *Ultrasound Med. Biol.*, 34(4):617–629, 2008.

[7] K Bhatia, C Cho, C Tong, E Yuen, and A Ahuja. Shear wave elasticity imaging of cervical lymph nodes. *Ultrasound in Medicine and Biology*, 30:195–201, 2012.

[8] M F Bieniosek, B J Lee, and C S Levin. Technical note: characterization of custom 3d printed multimodality imaging phantoms. *Medical Physics*, 42(10), 2015.

[9] A Bjrck. *Numerical methods for least squares problems.* SIAM, Philadelphia, 1996.

[10] D Blythe. The rise of the gpu. In *Proceedings of the IEEE*, volume 96(5), 2008.

[11] J C Bosshard, N Yallapragada, M P McDougall, and S M Wright. High speed mr elastography using sea imaging. In *16th Annual Meeting of the ISMRM*, 2008.

[12] C A Cantrell. Technical note: Review of methods for linear least-squares fitting of data and application to atmospheric chemistry problems. *Atmos. Chem. Phys.*, 8:5477–5487, 2008.

[13] Chris Cecka, Adrian J Lew, and E Darve. Assembly of finite element methods on graphics processors. *International Journal for Numericall Methods in Engineering*, 85(5):640–669, 2011.

[14] A Chaudhry, G Unnikrishnan, J N Reddy, T A Krouskop, and R Righetti. Effect of permeability on the performance of elastographic imaging techniques. *IEEE Transactions on Medical Imaging*, 32(2):189 – 199, 2013.

[15] Shuai Che, Michael Boyer, Jiayuan Meng, David Tarjan, Jeremy W Sheaffer, and Kevin Skadron. A performance study of general-purpose applications on graphics processors using cuda. *Journal of Parallel and Distributed Computing*, 68(10):1370–1380, 2008.

[16] P Chiarelli, B Vinci, A Lanata, V Gismondi, and S Chiarelli. Ultrasound poroelastic tissue typing. *Open Journal of Acoustics*, 1(6):55 – 62, 2011.

[17] Aidan J Cloonan, Danial Shahmirzadi, Ronny X Li, Barry J Doyle, Elisa E Konofagou, and Tim M McGloughlin. 3d printed tissue-mimicking phantoms

for medical imaging and computation validation applications. *3d Printing and Additive Manufacturing*, 1, 2014.

[18] S C Cowin and S B Doty. *Tissue Mechanics*. Springer Science, New York, New York, 2007.

[19] T Deffieux, G Montaldo, M Tanter, and M Fink. Shear wave spectroscopy for in vivo quantification of human soft tissue viso-elasticity. *IEEE Transactions in Medical Imaging*, 28:313 – 322, 2009.

[20] E E Drakonaki, G M Allen, and D J Wilson. Ultrasound elastography for musculoskeletal applications. *The British Journal of Radiology*, 85:1435–1445, 2012.

[21] Anders Eklund, Paul Dufort, Daniel Forsberg, and Stephen M LaConte. Medical image processing on the gpu - past, present and future. *Medical Image Analysis*, 17(8):1073 – 1094, 2013.

[22] A Evans, P Whelehan, K Thomson, D McLean, K Brauer, and C Purdie. Quantitative shear wave ultrasound elastography: initial experience in solid breast masses. *Breast Cancer Res*, 12:R104, 2010.

[23] G Ferraioli, C Tinelli, B Dal Bello, M Zicchetti, G Filice, and Filice C. Accuracy of real-time shear wave elastography for assessing liver fibrosis in chronic hepatitis c: a pilot study. *Hepatology*, 56:2125 – 2133, 2012.

[24] Y C Fung. *Biomechanics-Mechanical Properties of Living Tissues*. Springer-Verlag, NY, 2 edition, 1993.

[25] B S Garra, E I Cespedes, J Ophir, R S Spratt, R A Zuubier, C M Magnant, and M F Pennanen. Elastography of breast lesions: initial clinical results. *Radiology*, 202:79–86, 1997.

[26] J Gennisson, T Baldeweck, M Tanter, M S Catheline, M Fink, and L Sandrin. Assessment of elastic parameters of human skin using dynamic elastography. *IEEE Trans Ultrason Ferrolectr Freq Control*, 51:980 – 989, 2004.

[27] D T Ginat, S V Destounis, R G Barr, B Castaneda, J G Strang, and D J Rubens. Us elastography of breast and prostate lesions. *RadioGraphics*, 29:2007–2016, 2009.

[28] S Goenezen, J F Dord, Z Sink, P E Barbone, J Jiang, T J Hall, and A A Oberai. Linear and nonlinear elastic modulus imaging: An application to breast cancer diagnosis. *IEEE Transaction on Medical Imaging*, 31(8):1628 – 1637, 2012.

[29] Arthur S Goldberger. *A Course in Econometrics*. Harvard University Press, Cambridge, Massachusetts, 1991.

[30] R C Gonzalez and R E Woods, editors. *Digital Image Processing*. Prentice Hall, Upper Saddle River, New Jersey, 3 edition, 2008.

[31] Y Hong, X Liu, Z Li, X Zhang, M Chen, and Z Luo. Real-time ultrasound elastography in the differential diagnosis of benign and malignant thyroid nodules. *J Ultrasound Med*, 28:861–867, 2009.

[32] A Itoh, E Ueno, E Tohno, H Kamma, H Takahashi, T Shiina, M Yamakawa, and T Matsumura. Breast disease: clinical application of us elastography for diagnosis. *Radiology*, 239(2):341–50, 2006.

[33] M Januszewski and M Kostur. Accelerating numerical solustion of stochastic differential equations with cuda. *Computer Physics Communications*, 181(1):183–188, 2010.

[34] Grand Roman Joldes, Adam Witteck, and Karol Miller. Real-time nonlinear finite element computations on gpu - application no neorosurgical simulation.

Computer Methods in Applied Mechanics and Engineering, 199:3305–3314, 2010.

[35] R S Khandpur. *Handbook of analytical instruments.* Tata McGraw-Hill, New Delhi, 2 edition, 2006.

[36] Dieter Klatt, Sebastian Papazoglou, Jurgen Braun, and Sack Ingolf. Viscoelasticity-based mr elastography of skeletal muscle. *Phys. Med. Biol.*, 55:6445–6459, 2010.

[37] E E Konofagou, T Harrigan, and J Ophir. Shear strain estimation and lesion mobility assessment in elastography. *Ultrasonics*, 38(1-8):400–404, 2000.

[38] E E Konofagou, T P Harrigan, J Ophir, and T A Krouskop. Poroelastography: imaging the poroelastic properties of tissues. *Ultras. Med. Biol.*, 27:1387–1397, 2001.

[39] E E Konofagou and J Ophir. A new elastographic method for estimation and imaging of lateral displacements, lateral strains, corrected axial strains and poisson's ratios in tissues. *Ultrasound in Medicine and Biology*, 24(8):1183 – 1199, 1998.

[40] T A Krouskop, S Vinson, B Goode, and D Dougherty. A pulsed doppler ultrasonic system for making noninvasive measurements of the mechanical properties of soft tissue. *J. Rehab. Res. Dev.*, 24:1–8, 1987.

[41] K Kumar. Measurement of viscoelastic properties of polyacrylamide-based tissue-mimicking phantoms for ultrasound elastography applications. *IEEE Transactions on Instrumentation and Measurement*, 59(5):1224 – 1232, 2010.

[42] R S Lakes. *Viscoelastic Solids.* CRC Press, USA, 1999.

[43] E A Laws. *Mathematical methods for oceanographers: an introduction.* John Wiley & Sons, New York, 1997.

[44] L R Lines and S Treitel. Tutorial a review of least-squares inveresion and its application to goephysical problems. *Geophysical Prospecting*, 32:159 – 186, 1984.

[45] D Liu and E S Ebbini. Viscoelastic property measurement in thin tissue constructs using ultrasound. *IEEE Trans Ultrason Ferroelectr Freq Control*, 55(2):368–383, 2008.

[46] MD McGarry, EE Van Houten, PR Perriñez, AJ Pattison, JB Weaver, and KD Paulsen. An octahedral shear strain-based measure of snr for 3d mr elastography. *Physics in Medicine and Biology*, 56(13):153–164, 2011.

[47] Michael Milosevic, Sarah Jane Lunt, Julia Skliarenko, and Patricia Shaw. Interstitial permeability and elasticity in human cervix cancer. *Microvascular Research*, 75(3):381 – 390, 2008.

[48] Sanjay Padmanabhan Nair. Performance analysis of a new ultrasound axial strain time constant estimation. Master's thesis, TAMU, 2010.

[49] Sanjay Padmanabhan Nair and Raffaella Righetti. Resimulation of noise: a precision estimator for least square error curve-fitting tested for axial strain time constant imaging. *Physics in Medicine and Biology*, 60(9):3515–3529, 2015.

[50] Sanjay Padmanabhan Nair, Joshua Varghese, Anuj Chaudhry, and R Righetti. Effect of temporal acquisition parameters on image quality of strain time constant (tc) elastography. *Ultrasonic Imaging*, Accepted May 2014.

[51] Sanjay Padmanabhan Nair, Xu Yang, T A Krouskop, and R Righetti. Performance analysis of a new real-time elastographic time constant estimator. *IEEE Transactions on Medical Imaging*, 30(2):497–511, 2011.

[52] K Nightingale, S McAleavey, and G Trahey. Shear-wave generation using acoustic radiation force: in vivo and ex vivo results. *Ultrasound in Medicine and Biology*, 29:1715–1723, 2003.

[53] J Ophir, K Alam, B Garra, F Kallel, TA Krouskop, and T Varghese. Elastography: Ultrasonic estimation and imaging of the elastic properties of tissues. *Proc Inst Mech Eng*, H:1–31, 1999.

[54] J Ophir, I Cespedes, H Ponnekanti, Y Yazdi, and X Li. Elastography: a method for imaging the elasticity of biological tissues. *Ultrasonic Imaging*, 13(2):111–134, 1991.

[55] KJ Parker, MM Doyley, and DJ Rubens. Imaging the elastic properties of tissue: the 20 year perspective. *Physics in Medicine and Biology*, 56(1):R1 – R29, 2011.

[56] PR Perriñez, FE Kennedy, EE Van Houten, JB Weaver, and KD Paulsen. Magnetic resonance poroelastography: an algorithm for estimating the mechanical properties of fluid-saturated soft tissues. *IEEE Transactions on Medical Imaging*, 29(3):746–755, 2010.

[57] Y Qiu, M Sridhar, J K Tsou, K Lindfors, and M Insana. Ultrasonic viscoelasticity imaging of nonpalpable breast tumors: Preliminary results. *Acad Radiol*, 15:1526–1533, 2008.

[58] A Ranganathan. The levenberg-marquardt algorithm, 2004.

[59] S Raza, A Odulate, E M W Ong, S Chikarmane, and C W Harston. Using real-time tissue elastography for breast lesion evaluation. *J Ultrasound Med*, 29:551–563, 2010.

[60] J N Reddy. *An introduction to the finite element method*. McGraw-Hill, New York, 2006.

[61] R Righetti, B S Garra, L M Mobbs, C M Kraemer-Chant, J Ophir, and T A Krouskop. The feasibility of using poroelastographic techniques for distinguishing between normal and lymphedematous tissues in vivo. *Phys. Med. Biol.*, 52(21):6525–6541, 2007.

[62] R Righetti, J Ophir, B S Garra, R M Chandrasekhar, and T A Krouskop. A new method for generating poroelastograms in noisy environments. *Ultrasonic Imag.*, 27(201-211), 2005.

[63] R Righetti, J Ophir, and T A Krouskop. A method for generating permeability elastograms and poissons ratio time-constant elastograms. *Ultras. Med. Biol.*, 31(6):803–816, 2005.

[64] R Righetti, J Ophir, S Srinivasan, and T A Krouskop. The feasibility of using elastography for imaging the poissons ratio in porous media. *Ultrasound Med. Biol.*, 30:215–228, 2004.

[65] R Righetti, M Righetti, J Ophir, and T A Krouskop. The feasibility of estimating and imaging the mechanical behavior of poroelastic materials using axial strain elastography. *Phys. Med. Biol.*, 52(11):3241–3259, 2007.

[66] R Righetti, S Srinivasan, and J Ophir. Lateral resolution in elastography. *Ultrasound in Medicine and Biology*, 29(5):695–704, 2003.

[67] R Righetti, S Srinivasan, Kumar A Thitai, J Ophir, and T A Krouskop. Assessing image quality in effective poissons ratio elastography and poroelastography part i. *Physics Med. Biol.*, 52:1303–1320, 2007.

[68] I Sack, B Beierbach, U Hamhaber, D Klatt, and J Braun. Non-invasive measurement of brain viscoelasticity using magnetic resonance elastography. *NMR Biomed.*, 21(3):265–271, 2008.

[69] M H Sadd. *Elasticity: Theory, Application, and Numerics.* Academic Press, Boston, 2005.

[70] Yu P Samarin. Construction of exponential approximations for creep curves by the method of successive separation of exponential components. *Probl. Prochn.*, 9:24–27, 1974.

[71] J C Sarron, C Blondeau, A Guillaume, and D Osmont. Identification of linear viscoelastic constitutive models. *J Biomechanics*, 33:685–693, 2000.

[72] A Sarvazyan, T J Hall, M W Urban, M Fatemi, S R Aglyamov, and B S Garra. An overview of elastography - an emerging branch of medical imaging. *Current medical imaging reviews*, 7:255–282, 2011.

[73] M Sridhar and M F Insana. Ultrasonic measurements of breast viscoelasticity. *Med Phys.*, 34(12):4757–4767, 2007.

[74] M Sridhar, J Liu, and M F Insana. Viscoelasticity imaging using ultrasound: parameters and error analysis. *Physics in Medicine and Biology*, pages 2425–2443, 2007.

[75] S Srinivasan, T A Krouskop, and J Ophir. Comparing elastographic strain images with modulus images obtained using nanoindentation: preliminary results using phantoms and tissue samples. *Ultrasound Med. Biol.*, 30(3):329–343, 2004.

[76] S Srinivasan, R Righetti, and J Ophir. Trade-offs between the axial resolution and the signal-to-noise ratio in elastography. *Ultrasound Med Biol*, 29(6):847–866, 2003.

[77] M Swiatkowska-Freund and K Preis. Elastography of the uterine cervix: implications for success of induction of labor. *Ultrasound Obstet Gynecol*, 38:52–56, 2011.

[78] M Tanter, J Bercoff, T Athanasiou A, Deffieux, J L Gennisson, G Montaldo, M Muller, A Tardivon, and M Fink. Quantitative assessment of breast lesion viscoelasticity: Initial clinical results using supersonic shear imaging. *Ultrasound in Medicine and Biology*, 34:1373 – 1386, 2008.

[79] K Terzaghi and R B Peck. *Soil Mechanics in Engineering Practice*. John Whiley and Sons, New York, 1966.

[80] A Thomas, S Kümmel, F Fritzche, M Warm, B Ebert, B Hamm, and T Fischer. Real-time sonoelastography performed in addition to b-mode ultrasound and mammography: improved differentiation of breast lesions. *Acad Radiol*, 13:1496–1504, 2006.

[81] A Thomas, M Warm, M Hoopmann, F Diekmann, and T Fischer. Tissue doppler and strain imaging for evaluating tissue elasticity of breast lesions. *Acad Radiol*, 14:522–529, 2007.

[82] Joshua Varghese. Effect of temporal acquisition parameters on the image quality of ultrasound axial strain time-constant elastograms. Master's thesis, TAMU, 2011.

[83] T Varghese and J Ophir. A theoretical framework for performance characterization of elastography: The strain filter. *IEEE Trans. Ultras. Ferroel. Freq. Cont.*, 44(1):164–172, 1997.

[84] P N T Wells and H D Liang. Medical ultrasound: imaging of soft tissue strain and elasticity. *J R Soc Interface*, 8:1521 – 1549, 2011.

[85] J Wu. Tofu as a tissue-mimicking material. *Ultras Med Biol.*, 27:1297–1300, 2001.

[86] Yuan Ya-Xiang. Recent advances in numerical methods for nonlinear equations and nonlinear least squares. *Numerical Algebra, Control and Optimization*, 1(1):15–34, 2011.

[87] M Yamakawa and T Shiina. Tissue viscoelasticity imaging using vibration and ultrasound coupler gel. *Japanese Journal of Applied Physics*, 51(7):07GF12, 2012.

[88] X Yang, S Deka, and R Righetti. Elastography on gpgpu for real-time applications. In *Proceedings of the 8th International Conference on the ultrasonic measurement and imaging of tissue*, Vlissingen, Zeeland, The Netherlands, 2009.

[89] H Zhi, B Ou, B M Luo, X Feng, Y L Wen, and H Y Yang. Comparison of ultrasound elastography, mammography, and sonography in the diagnosis of solid breast lesions. *J Ultrasound Med*, 26:807–815, 2007.